

# Radial evolution of the April 2020 stealth coronal mass ejection between 0.8 and 1 AU

## Comparison of Forbush decreases at Solar Orbiter and near the Earth

Johan L. Freiherr von Forstner<sup>1</sup>, Mateja Dumbović<sup>2</sup>, Christian Möstl<sup>3</sup>, Jingnan Guo<sup>4,5,1</sup>, Athanasios Papaioannou<sup>6</sup>, Robert Elftmann<sup>1</sup>, Zigong Xu<sup>1</sup>, Jan Christoph Terasa<sup>1</sup>, Alexander Kollhoff<sup>1</sup>, Robert F. Wimmer-Schweingruber<sup>1</sup>, Javier Rodríguez-Pacheco<sup>7</sup>, Andreas J. Weiss<sup>3</sup>, Jürgen Hinterreiter<sup>3</sup>, Tanja Amerstorfer<sup>3</sup>, Maike Bauer<sup>3</sup>, Anatoly V. Belov<sup>8</sup>, Maria A. Abunina<sup>8</sup>, Timothy Horbury<sup>9</sup>, Emma E. Davies<sup>9</sup>, Helen O'Brien<sup>9</sup>, Robert C. Allen<sup>10</sup>, G. Bruce Andrews<sup>10</sup>, Lars Berger<sup>1</sup>, Sebastian Boden<sup>1,11</sup>, Ignacio Cernuda Cangas<sup>7</sup>, Sandra Eldrum<sup>1</sup>, Francisco Espinosa Lara<sup>7</sup>, Raúl Gómez Herrero<sup>7</sup>, John R. Hayes<sup>10</sup>, George C. Ho<sup>10</sup>, Shrinivasrao R. Kulkarni<sup>1,12</sup>, W. Jeffrey Lees<sup>10</sup>, César Martín<sup>1,13</sup>, Glenn M. Mason<sup>10</sup>, Daniel Pacheco<sup>1</sup>, Manuel Prieto Mateo<sup>7</sup>, Ali Ravanbakhsh<sup>1,14</sup>, Oscar Rodríguez Polo<sup>7</sup>, Sebastián Sánchez Prieto<sup>7</sup>, Charles E. Schlemm<sup>10</sup>, Helmut Seifert<sup>10</sup>, Kush Tyagi<sup>15</sup>, and Mahesh Yedla<sup>1,14</sup>

(Affiliations can be found after the references)

March 2, 2021

### ABSTRACT

**Aims.** We present observations of the first coronal mass ejection (CME) observed by the Solar Orbiter spacecraft on April 19, 2020 and the associated Forbush decrease (FD) measured by the High Energy Telescope (HET). This CME is a multi-spacecraft event that was also seen near Earth the following day.

**Methods.** We highlight the capabilities of the HET for observing small short-term variations of the galactic cosmic ray count rate using its single detector counters. We applied the analytical ForbMod model to the FD measurements to reproduce the Forbush decrease at both locations. Input parameters for the model were derived from both in situ and remote-sensing observations of the CME.

**Results.** The very slow ( $\sim 350$  km/s) stealth CME caused an FD with an amplitude of 3 % in the low-energy cosmic ray measurements at HET and 2 % in a comparable channel of the Cosmic Ray Telescope for the Effects of Radiation (CRA TER) on board the Lunar Reconnaissance Orbiter, as well as a 1 % decrease in neutron monitor measurements. Significant differences are observed in the expansion behavior of the CME at different locations, which may be related to influence of the following high speed solar wind stream. Under certain assumptions, ForbMod is able to reproduce the observed FDs in low-energy cosmic ray measurements from HET as well as CRA TER, however, with the same input parameters, the results do not agree with the FD amplitudes at higher energies measured by neutron monitors on Earth. We study these discrepancies and provide possible explanations.

**Conclusions.** This study highlights the notion that the novel measurements of Solar Orbiter can be coordinated with observations from other spacecraft to improve our understanding of space weather in the inner heliosphere. Multi-spacecraft observations combined with data-based modeling are also essential for understanding the propagation and evolution of CMEs, in addition to their space weather impacts.

**Key words.** Sun: coronal mass ejections (CMEs) - Sun: heliosphere - cosmic rays

## 1. Introduction

On April 19, 2020, a coronal mass ejection (CME) passed Solar Orbiter (SolO, Müller et al. 2020) spacecraft, making it the first large-scale flux rope CME seen in situ at SolO. At this time, the spacecraft was closely aligned in heliospheric longitude with Earth (less than  $4^\circ$  separation) and it was located at a radial distance of 0.8 AU from the Sun, as shown in Fig. 1. Consequently, the same slow CME ( $v < 400$  km/s) was also observed near Earth the next day, causing the first geomagnetic storm of the year with a Dst index of  $-59$  nT and Kp index of 5. During the event, SolO was still in its Near Earth Commissioning Phase (NECP), which ended on June 15, 2020; nevertheless, some of the in situ instruments, including the Energetic Particle Detector suite (EPD, Rodríguez-Pacheco et al. 2020) and the magnetometer (MAG, Horbury et al. 2020) were already taking continuous measurements and were able to observe signatures of the CME. In addition, the STEREO-A spacecraft had a sufficient longitudinal separation of  $\sim 75^\circ$  from SolO and the Earth, thus, making it

capable of providing excellent remote sensing observations of the CME propagation from a side view. This event was observed from both SolO and the Earth, providing an excellent example for the coordinated science that is possible with SolO and other heliophysics missions in the Solar System.

Clouds of magnetized plasma ejected from the Sun, known as CMEs, are one of the key phenomena in space weather research, as they can cause severe geomagnetic storms (Kilpua et al. 2017) that disrupt the terrestrial infrastructure. The shocks driven by CMEs are also partly responsible for energetic particles in the heliosphere (Reames 2013), which may pose radiation danger to astronauts and spacecraft. Consequently, two of the four main scientific questions of the Solar Orbiter mission (Müller et al. 2013) are also linked to the goal of attaining a better understanding of CMEs.

Forbush decreases (FDs), first observed by and later named after Scott E. Forbush (1937), are short-term decreases of the galactic cosmic ray (GCR) flux, caused by the passage of mag-

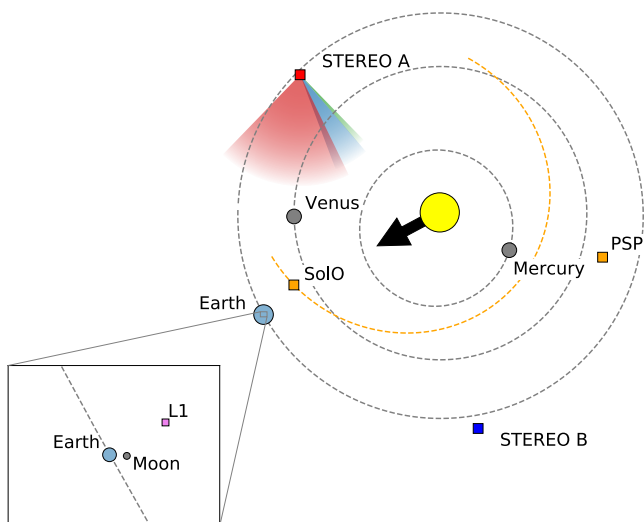


**Fig. 1.** Locations of planets and spacecraft in the inner solar system on April 20, 2020, the day the CME arrived in the vicinity of Earth. The trajectory of Solar Orbiter (SolO) is shown as an orange dashed line and PSP denotes the location of Parker Solar Probe. The large black arrow indicates the approximate propagation direction of the CME and the colored segments next to STEREO-A show the fields of view of the remote sensing instruments COR1/COR2 (green), HI1 (blue), and HI2 (red). The inset shows a zoomed-in view of the relative positions of Earth, the Moon, and the Lagrange point L1, where the Wind spacecraft is located.

netic field structures in the solar wind, such as CMEs or stream interaction regions (SIRs). Such magnetic structures can act as a barrier for the propagation of GCRs, as, for instance, the GCRs need to diffuse across a strong field, so that the observed flux is temporarily decreased at the locations where these structures pass. The decrease phase usually takes less than one day, followed by an often slower recovery to the previous level (on the order of one week). In the case of CMEs, FDs are driven by both the turbulent shock-sheath region (if present) as well as the following magnetic ejecta; these are two effects that can sometimes be clearly separated when a two-step decrease is observed (e.g., Cane 2000). The amplitude of an FD depends not only on the properties of the heliospheric structure, but also on the energy of the observed GCR particles: lower energy particles are modulated more easily and thus tend to show larger FDs (e.g., Lockwood 1971; Lockwood et al. 1991; Cane 2000; Guo et al. 2020). In the past, the study of FDs was mainly based on data from neutron monitors on the surface of the Earth, but nowadays, GCR measurements suitable for FD studies are also available from many spacecraft in the near-Earth space as well as on other solar system bodies and these have been routinely used for multi-spacecraft studies (e.g., Cane et al. 1994; Lockwood et al. 1991; Freiherr von Forstner et al. 2018, 2019, 2020; Witasse et al. 2017; Winslow et al. 2018). In all cases, it is important to take into account the energy dependence of the FD amplitude, as such instruments may be sensitive to different GCR energies.

In this work, we present the EPD observations of the FD associated with the April 19 CME at SolO, as well as the corresponding observations at Earth. We describe which EPD data products are best suited to make measurements of FDs, and we analyze these data to see how the CME affected the GCR flux at different heliospheric locations and at different particle energies. We also employ the ForbMod model to reproduce the observed

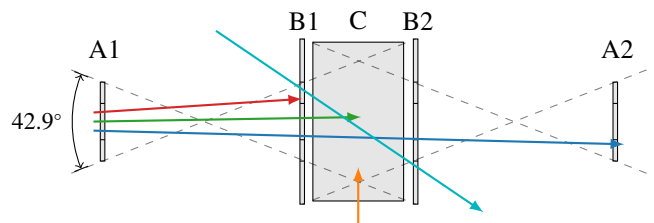


**Fig. 2.** Schematic diagram of the HET sensor head. Exemplary particle trajectories ending up in different data products are shown by the arrows: **stopping in B**, **stopping in C**, **penetrating**, GCR channel, **C single counter**. A 3D graphic of the sensor head is shown in Rodríguez-Pacheco et al. (2020, Fig. 31).

FD and gain insight into the how the large-scale evolution of the CME structure affected the properties of the FD. One study from Davies et al. (2021) complements this work by investigating the magnetic field measurements at both Solar Orbiter and Earth in more detail. In Sect. 2, we introduce the different instruments used as data sources in this study, followed by an overview of our modeling methods in Sect. 3. The measurement and modeling results are presented in Sect. 4 and then discussed in more detail in Sect. 5.

## 2. Data sources

### 2.1. HET on Solar Orbiter

As part of the EPD suite (Rodríguez-Pacheco et al. 2020) on board the Solar Orbiter mission (Müller et al. 2013; Müller et al. 2020), the High Energy Telescope (HET) is a particle telescope covering the high-energy end of the solar energetic particle (SEP) spectrum as well as galactic cosmic rays (GCR). Its two double-ended telescopes each consist of four thin 300  $\mu\text{m}$  silicon solid-state detectors (named the A1, B1, B2, and A2 detectors) and the C detector, a 2 cm thick  $\text{Bi}_4\text{Ge}_3\text{O}_{12}$  (BGO) scintillator, in the center. This detector layout is shown in Fig. 2. The C detector is read out using two photodiodes placed on either side, named C1 and C2. HET is designed to measure the fluxes of electrons above 300 keV, protons above 7 MeV, as well as heavier ions, with one telescope (HET1) providing the sunward and anti-sunward viewing directions (parallel to the mean Parker spiral angle); and with the other telescope (HET2) being mounted perpendicular to HET1 in order to measure particles coming from outside the ecliptic plane. The telescopes distinguish between particles stopping in one of the B detectors (B1 or B2, e.g., red arrow in Fig. 2), particles stopping in the C (green arrow) detector, and particles penetrating the whole telescope (blue arrow) to achieve a large energy coverage; in addition, they use the  $dE/dx$ - $E$ -method to separate different particle species. This technique has been applied in many earlier space-borne charged particle detectors, including the Interplanetary Monitoring Platform-1 mission in the 1960s (McDonald & Ludwig 1964) as well as more recent instruments, such as the Mars Science Laboratory Radiation Assessment Detector (Hassler et al. 2012) and the Chang'E 4 Lunar Lander Neutrons and Dosimetry experiment (Wimmer-Schweingruber et al. 2020). For more details about the application of the  $dE/dx$ - $E$ -method in HET, see Rodríguez-Pacheco et al. (2020, Sect. 7.2.5).

While the nominal data products of HET are optimized for the study of high intensity SEP events by choosing a rather small opening angle to achieve a high energy resolution, these data are not optimal for observing short-term variations of the GCR

background due to their low level of counting statistics. Alternatively, HET provides a separate “GCR channel” that observes penetrating particles with a larger opening angle by omitting the A detectors from the coincidence condition, namely, by counting all particles that penetrate B1, C, and B2 (e.g., teal arrow in Fig. 2). This leads to an almost 20-fold increase in the geometric factor compared to the nominal penetrating particle channel.

For applications requiring even higher counting statistics, it is also possible to use single detector count rates without any coincidence conditions, similar to the technique applied, for instance, by Richardson et al. (1996) for the IMP 8 and Helios E6 instruments and Kühl et al. (2015) for SOHO-EPHIN. In this case, GCR particles are measured from all directions (e.g., orange arrow in Fig. 2), but without any energy resolution or species separation. The HET C detectors are best suited for this purpose due to their large size and nearly isotropic shielding by the aluminum housing. For each HET telescope, four such counters are available, where each of the two photodiodes has a high-gain channel (C1H, C2H), with a deposited energy threshold of  $E_{th} = 4$  MeV, and a low-gain channel (C1L, C2L), with  $E_{th} = 10$  MeV. As these C detector counters provide no directional information, the values from HET 1 and HET 2 and from the two photodiodes in each telescope can be simply summed up to achieve an even higher count rate, that is, approximately 270 counts/s for the high-gain channels (C1H + C2H  $\times$  2 units) or 230 counts/s for the low-gain channels (C1L + C2L  $\times$  2 units). We note that summing up the counts of the two photodiodes does not remove events that were detected in both photodiodes at the same time as such a counter of all valid events in the C detector is not available in the HET data products and could only be approximated using the pulse height analysis data.

To investigate the response of the HET C counters to an isotropic flux of incoming GCR particles, we performed a simulation using Geant4 (Agostinelli et al. 2003), version 10.1.2, with the physics list QGSP\_BERT. The simulated geometry included a detailed model of the EPT-HET sensor head and the corresponding electronics box, so that the shielding by the instrument housing and electronics box, as well as the generation of secondary particles, are taken into account. A simplified model of the Solar Orbiter spacecraft was also optionally included in the simulation setup to consider the influence of the spacecraft body on the incoming particle flux. This may be important for the C detector counters, as they are sensitive to particles entering HET from any direction. The spacecraft was modeled as a cuboid with the size of the main body (2.20 m  $\times$  1.81 m  $\times$  1.46 m) and total mass of 1700 kg (which corresponds to the launch mass of Solar Orbiter, excluding its solar panels). Its composition was assumed to be 200 kg of hydrazine fuel, 750 kg of aluminum representing the structural components of the spacecraft, and 750 kg of a printed circuit board (PCB)-like material, as defined by Appel et al. (2018) and Appel (2018, Table 6.2) representing the electronics components of the spacecraft and its payload. The development of a more detailed Geant4 model of the spacecraft body based on CAD models of its components is in progress, but was not possible within the time constraints of this study and is not expected to change the results significantly. Only protons between 5 MeV and 100 GeV were used as input particles to reduce the complexity of the simulation setup, as protons comprise 90 % of primary GCR particles (Simpson 1983).

The proton response function resulting from the simulation is shown in Fig. 3 (upper panel). Four curves are shown, corresponding to the simulation setup with and without the spacecraft model, and for the different threshold energies of the high- and low-gain channels. It becomes clear that the low-energy cutoff

is mainly influenced by the threshold energy: 12 MeV for the high-gain channel and 16 MeV for the low-gain channel. After the cutoff follows a narrow plateau corresponding to particles entering C through the nominal field of view (i.e., through the A and B detectors), followed by an increase related to particles entering from the sides through the HET housing. The spacecraft body provides additional shielding ( $\sim 20$  %) for the detector in the lower energy part, but generates additional secondary particles above a primary proton energy of 1 GeV — up to a 2.5-fold increase in the geometric factor for 100 GeV particles. On the other hand, without the spacecraft body, the geometric factor for high energies stays approximately constant above 1 GeV, at  $G = (128 \pm 2) \text{ cm}^2 \text{ sr}$  for  $E_{th} = 4$  MeV and  $G = (106 \pm 2) \text{ cm}^2 \text{ sr}$  for  $E_{th} = 10$  MeV. As the GCR proton flux typically peaks at or below 1 GeV and decreases again for higher energies, the differences caused by the spacecraft body only exert a minor influence on the observed count rates. By folding the response function for  $E_{th} = 4$  MeV with a typical GCR spectrum at solar minimum ( $\Phi = 270$  MV) and integrating over the primary energy, we obtained count rates of 48/s without the spacecraft model and 53/s with the spacecraft model, an increase on the order of 10 %. This is only about 80 % of the typically observed count rate (270/s, divided among four channels), as only protons were simulated. We note that the effect of the spacecraft body may be larger for heavier ions, as they fragment more in the spacecraft and may thus contribute more to the response function with the generated secondaries.

## 2.2. CRaTER on LRO

The Cosmic Ray Telescope for the Effects of Radiation (CRaTER, Spence et al. 2010) is an instrument on the Lunar Reconnaissance Orbiter (LRO) mission measuring the radiation dose and linear energy transfer (LET) spectra in lunar orbit. CRaTER consists of three pairs of thin (140  $\mu\text{m}$ ) and thick (1000  $\mu\text{m}$ ) silicon detectors, D1 through D6, separated by sections of tissue-equivalent plastic serving as an absorber. The D1 end of the telescope is pointed towards the zenith, while the D6 end points towards the surface of the Moon. Similarly to HET, CRaTER uses multiple coincidence conditions between its detectors to measure particles of different energies. For example, the lowest energy particles are detected using the coincidence of D1 and D2 (the uppermost two detectors), with a minimum energy of 12.7 MeV required for protons to penetrate D1 and reach into D2 according to Spence et al. (2010). This value of 12.7 MeV is also the minimum energy for protons to be detected in any CRaTER detector, as D1 has a higher energy deposit threshold, so that it rejects most protons and many helium ions.

The CRaTER Level 2 secondary science data, available through NASA PDS<sup>1</sup> and on the CRaTER web site<sup>2</sup>, provide single counters for each of the six detectors, similar to the HET counters described in Sect. 2.1, as well as additional counters for “rejected events”, “good events”, and “total events”, where a good event is any valid event where an incoming particle triggered at least one detector.

This means that there are two different counters in the CRaTER data (D2 and good events) measuring protons with energies  $\geq 12.7$  MeV, while the threshold is higher for all other counters. The good events counter was already used by Sohn et al. (2019b,a) to study Forbush decreases and energetic particle events, and it has the best counting statistics (on the order of

<sup>1</sup> <https://pds-ppi.igpp.ucla.edu/>

<sup>2</sup> <http://crater-web.sr.unh.edu/>

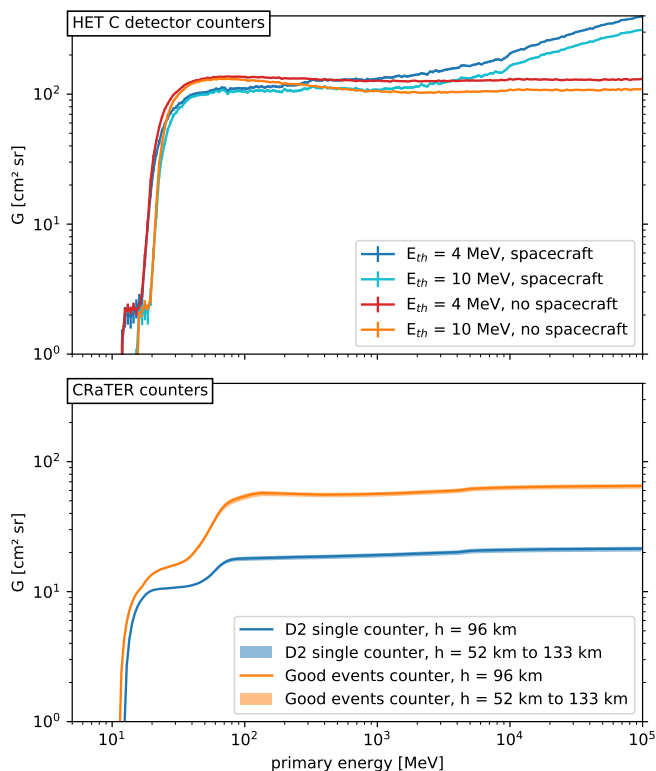


**Fig. 3.** Response functions (i.e. energy-dependent geometric factors) of the SoLo HET and LRO CRaTER detectors employed to measure FDs in this study. *Upper panel:* HET C detector single counters. The four lines correspond to four different scenarios depending on the threshold applied for the available counters. The derivation of the response function using a Geant4 simulation is described in Sect. 2.1. *Lower panel:* D2 detector single counter (blue) and *good events* counter (orange) of CRaTER. Lines show the response for the mean altitude of CRaTER during the event, while shaded areas mark the range of responses for the maximum and minimum altitudes. These response functions were derived by Looper et al. (2013) and are described in Sect. 2.2.

$\sim 66/s$  at the time of the event studied here). However, while the threshold is well defined, the response function of the good events counter is slightly more complex, as it includes multiple detectors with different shielding conditions and measures a higher amount of secondary particles coming from the lunar surface (the so-called albedo) than D2 alone. Looper et al. (2013, Appendix A) derived the response functions of the single detector count rates using a Geant4 (Agostinelli et al. 2003) simulation. The response functions of the D2 detector single counter as well as the good events counter are plotted in Fig. 3 (lower panel). Similarly to the HET response function in the upper panel, steps in the response function occur when different parts of the telescope are penetrated by particles.

In addition to the count rate files, we used the ancillary data of the LRO to exclude time periods where the spacecraft is not in its nominal orientation, for instance, due to orbit adjustment maneuvers. Any data where the LRO is more than  $1^\circ$  away from the nominal orientation, with CRaTER’s D2 detector pointing towards the zenith, is excluded to make sure that the measured count rates are not affected by these activities. This exclusion only affects few data points, as the LRO pointing is usually very precise to support its imaging instruments.

As the LRO orbit is elliptical and relatively close to the lunar surface (between 54 km and 132 km above the surface in the

time period studied in this work), the Moon takes up a significant portion of the sky as viewed from CRaTER. Thus, the Moon shields CRaTER from part of the incoming GCR, but also produces albedo particles. This means that the count rate of particles measured using a single-detector counter (i.e., in a  $4\pi$  solid angle field of view) periodically varies with the current altitude, which is also shown in the altitude-dependent response functions in Fig. 3 (lower panel). The plotted altitudes are slightly different from the actual values ( $\pm 2$  km) due to the limited altitude resolution of the simulation, but this only makes a small difference. The orbital period of the LRO is about 110 minutes, which determines the frequency of this periodic signal. Multiple methods have been developed to correct for this effect, such as the dose correction factor given by Schwadron et al. (2012) based on geometrical calculation of the covered solid angle, or the Fourier series method introduced by Winslow et al. (2018). In this study, we apply a simple empirical method in which we create a scatter plot of the time-dependent CRaTER count rate  $c(t)$  versus the LRO altitude  $h(t)$  for the time period of interest, apply a linear regression, and use the obtained slope  $m$  to calculate the corrected count rate

$$c_{\text{corrected}}(t) = c(t) - m \cdot (h(t) - \bar{h}), \quad (1)$$

where  $\bar{h}$  denotes the mean altitude of the LRO during the time period investigated, which is 93 km for the event studied in this work. In this case, we found this method to work about as well as the Fourier series method in suppressing the periodic signal and better than the simple geometrical calculation, which does not take into account the albedo particles generated by the Moon. However, short- or long-term variations of the GCR spectrum, which influence the ratio between the counts of primary GCR and albedo particles, and thus the necessary correction factor, are not accounted for by any of these methods and can still cause the periodic component to appear in the corrected signal, albeit with a much lower amplitude. Due to these difficulties with the altitude correction, we additionally always plot orbit-averaged values of the CRaTER data.

### 2.3. Neutron monitor observations and the global survey method

As stated above, neutron monitors have historically been the most important data source for the study of GCR variations in general and FDs in particular. The global network of neutron monitors, whose data are available from the Neutron Monitor Database (NMDB)<sup>3</sup>, provides continuous measurements from many locations around the globe. In contrast to deep space measurements, neutron monitors have an inherent cutoff energy (often given in terms of rigidity) determined by the Earth’s magnetosphere and atmosphere, which depends on the latitude as well as the altitude of the neutron monitor. At the poles, the influence of the magnetosphere decreases to zero (see e.g., Smart & Shea 2008), leading to a cutoff rigidity of 0.1 GV at the location of the South Pole neutron monitor, which would correspond to a proton energy of  $\sim 5$  MeV. At these locations, the atmospheric cutoff dominates and results in a cutoff energy of about 450 MeV for protons Clem & Dorman (2000), that is, a factor of  $\sim 20$ – $30$  larger than in the abovementioned response functions of HET and CRaTER. This causes Forbush decreases observed by neutron monitors to usually be smaller in amplitude than in deep space observations.

<sup>3</sup> <http://www.nmdb.eu>



A method that takes into account simultaneous ground-level observations of cosmic rays by neutron monitors at different locations to calculate the main characteristics of cosmic-ray variations outside of the atmosphere and magnetosphere of Earth has long been proposed (see Krymsky 1964; Krymsky et al. 1966; Belov et al. 1973, 1974; Dorman 2009) and is still used nowadays (e.g., Papaioannou et al. 2019, 2020; Abunina et al. 2020). This technique is called the global survey method (GSM). The GSM separates the isotropic part of the variations of cosmic rays from the anisotropic part and uses spherical harmonics to express their respective amplitudes. In the following,  $A_0$  is used for the amplitude of the isotropic variations;  $A_x$ ,  $A_y$ , and  $A_z$  are the corresponding amplitudes of the first harmonic (higher orders are not considered). Here,  $A_x$  and  $A_y$  denote the equatorial components of the anisotropy, with  $x$  pointing away from the Sun and  $y$  perpendicular to that, while  $z$  is the north-south component. However, in order to achieve this, first the atmospheric and instrumental response functions, which couple the primary particles at the top of the atmosphere to the secondaries recorded by neutron monitors on the ground, and a backmapping of cosmic ray particles traveling under the influence of Earth's magnetic field are applied. The historical development, scientific argumentation, and mathematical formulation of the GSM can be found in the recent comprehensive report of Belov et al. (2018). The GSM incorporates a power-law dependence on the rigidity for the isotropic part of the CR variations (i.e.,  $A_0$ ) and thus can provide outputs for a set of fixed rigidities (see e.g., Figure 2 in Belov 2000). However, a fixed rigidity of 10 GV (corresponding to a proton energy of 9.1 GeV) has typically been used for more than 65 years (e.g., Belov 2000; Belov et al. 2015, 2018; Papaioannou et al. 2020; Abunina et al. 2020). This value is more illustrative on the actual GCR modulation and is close to the effective rigidity of NMs to detect GCRs (see e.g., Asvestari et al. 2017; Koldobskiy et al. 2018), implying that a NM is mostly responsive to the variability of mid-rigidity CRs from several GV to several tens of GV in rigidity.

### 3. ForbMod

ForbMod (Dumbović et al. 2018) is an analytical physics-based model to describe Forbush decreases caused by flux rope CMEs. Its calculations are based on the self-similar expansion of a flux rope, which is modeled as a (locally) cylindrical structure with an initial radius,  $a_0$ , close to the Sun that initially contains no GCRs at its center. While the flux rope propagates away from the Sun, it expands self-similarly: Both the increase in the flux rope radius  $a$  and the decrease in the central magnetic field magnitude  $B_c$  are assumed to follow power law expressions with the so-called expansion factors  $n_a$  and  $n_B$  used as power law indices:

$$a(t) = a_0 \left( \frac{R(t)}{R_0} \right)^{n_a}, \quad B_c(t) = B_0 \left( \frac{R(t)}{R_0} \right)^{-n_B}, \quad (2)$$

where  $R(t)$  describes the radial distance of the flux rope from the Sun,  $R_0$  the initial distance at time  $t = 0$ , and  $B_0$  the initial central magnetic field. As stated by Dumbović et al. (2018), previous observational studies (Bothmer & Schwenn 1998; Leitner et al. 2007; Démoulin et al. 2008; Gulisano et al. 2012) constrained the power law indices to  $0.45 < n_a < 1.14$  and  $0.88 < n_B < 1.89$ . During the expansion and radial propagation of the CME, the GCRs gradually diffuse into the flux rope slower than in the surrounding solar wind, so that the GCR phase space density within the flux rope is decreased while it passes by an observer.

ForbMod then describes the GCR phase space density within the flux rope using the following main equations, which are derived in detail by Dumbović et al. (2018):

$$U(r, t) = U_0 \left( 1 - J_0 \left( \alpha_1 \frac{r(t)}{a(t)} \right) e^{-\alpha_1^2 f(t)} \right), \quad f(t) = \frac{D_0}{a_0^2} \left( \frac{v}{R_0} \right)^x \frac{t^{x+1}}{x+1}, \quad (3)$$

where  $U_0$  is the GCR phase space density outside the flux rope,  $J_0$  is the Bessel function of the first kind and order zero,  $\alpha_1$  is a constant corresponding to the first positive root of  $J_0$ ,  $r$  is the radial distance of the observer from the flux rope center (which may be time-dependent, hence  $r(t)$ ),  $D_0$  is the initial diffusion coefficient, and  $v$  is the CME propagation speed. The function  $f(t)$  describes the GCR diffusion into the flux rope, where the diffusion time is equivalent to the propagation time  $t$  since the initial condition ( $t = 0$ ) near the Sun. It is assumed that  $v$  is constant and that the diffusion coefficient  $D$  is inversely proportional to the central magnetic field,  $D \propto 1/B_c$ , so that  $D(t)$  follows a power law with the index  $n_B$  (c.f. Eq. 2). This power law relation was already inserted to obtain the expression for  $f(t)$  given in Equation 3. Additionally, the ambient GCR phase space density,  $U_0$ , is assumed to be constant to simplify the calculation; the known radial gradient the GCR flux of about 3 %/AU (Webber & Lockwood 1999; Gieseler & Heber 2016; Lawrence et al. 2016) is not taken into account. The expansion type

$$x = n_B - 2n_a \neq -1 \quad (4)$$

describes the expansion behavior of the CME, and in particular its magnetic flux.  $x = 0$  corresponds to a conservation of magnetic flux (as the product of the flux rope cross section and the central magnetic field stays constant), while  $x > 0$  describes a decrease in the flux with heliospheric distance and  $x < 0$  an increasing flux.  $x = -1$  is a special case, which requires a different functional form of  $f(t)$  in Equation 3 (for details, see Dumbović et al. 2018). The influence of the value of  $x$  on the ForbMod result can be understood as the interplay between the expansion and diffusion effects – when the diffusion (which depends on the magnetic field, and thus,  $n_B$ ) is very efficient, the flux rope is quickly filled with GCR particles, but a fast increase in the flux rope size (large  $n_a$ ) can counteract this effect by increasing the space that needs to be filled with GCRs.

In addition to its dependence on the magnetic field, the GCR diffusion coefficient  $D$  also depends on the particle energy. For instance, higher energy particles diffuse into the flux rope more easily and thus show a shallower FD. While the original model of Dumbović et al. (2018) describes only the FD profile of one specific GCR energy, for which  $D_0$  needs to be provided, Dumbović et al. (2020) extended the model with empirical functions for the energy dependence of the diffusion coefficient, so that the FD profile can be calculated for any GCR energy. By folding the resulting spectrum with the response function of a particle detector, it is then possible to simulate the measurement of the FD by this detector. In this version of ForbMod, the input GCR spectrum and the energy dependence of the diffusion coefficient  $D$  are needed as input parameters for the model. As described by Dumbović et al. (2020, Appendix B), the modified force-field approximation described by Gieseler et al. (2017) is used to calculate the GCR spectrum based on the values of the solar modulation potential  $\Phi$  obtained from neutron monitor data by Usoskin et al. (2011) and from ACE/CRIS data by Gieseler et al. (2017). For our event in April 2020, near the minimum between Solar Cycles 24 and 25, the corresponding measurements of  $\Phi$

are not yet available, so we use the values from similar conditions for the previous solar cycle in June 2009. The values from Usoskin et al. (2011) are derived based on data from the Oulu neutron monitor; as its count rates between April 2020 and June 2009 are comparable, this supports our assumption that the solar modulation conditions are very similar. The energy-dependent diffusion coefficient is calculated using the empirical formula given by Potgieter (2013), with parameters derived by Potgieter et al. (2014) for the period 2006–2009 from PAMELA data and by Corti et al. (2019) for the period 2011–2017 from AMS-02 measurements. In this case, data for 2020 are not yet available either, so we use the values from 2009 with comparable solar cycle conditions. More detailed explanations about these parameters are given by Dumbović et al. (2020, Appendix A).

To convert the  $U(r, t)$  dependence in Equation 3 into a function that purely depends on the time,  $t$ , and can thus directly be compared to in situ GCR measurements, the observer location,  $r$ , with respect to the flux rope center, needs to be defined. For this, we can use the in situ measured velocity profile  $v_{\text{in situ}}(t)$  of the flux rope, namely, the observer passes through the flux rope at this measured velocity:

$$r(t) = |a(t) - v_{\text{in situ}}(t) \cdot (t - t_{\text{CME}})|, \quad (5)$$

where  $t_{\text{CME}}$  is the in situ arrival time of the CME. The conversion of  $U(r)$  into  $U(t)$  introduces some asymmetry into the FD profile, as the in situ measured velocity profile  $v_{\text{in situ}}(t)$  is typically not constant. We note that ForbMod only models the GCR modulation due to a flux rope CME, not the additional influence of a shock-sheath region, although it may be combined with other models to take this into account (see e.g., Dumbović et al. 2020; Freiherr von Forstner et al. 2020).

## 4. Results

### 4.1. In situ observations

The April 19 CME was observed at Solar Orbiter using its magnetometer, showing a clear signature of a flux rope with a south-east-north field rotation and a maximum field intensity of  $B_{\text{max}} = 21.2$  nT, a preceding shock with a jump of about 3 nT in magnetic field intensity, and a turbulent sheath region in between (see the upper panel in Fig. 4, and see Davies et al. (2021) for further discussion of the MAG data). The shock arrival time was 05:06 UTC on April 19, 2020, the flux rope arrived at 08:58 UTC on the same day and ended at 01:11 UTC on April 20. MAG data from April 21 (i.e., one day after the end of the CME flux rope) are not displayed here because spacecraft commissioning activities affected the sensor temperatures on that day. Solar wind plasma measurements from the Solar Wind Analyzer instrument on SolO (SWA, Owen et al. 2020) are not available for this event, as it was not yet fully commissioned. EPD measured the fluxes of suprathermal ions slightly above solar wind energies (5.3 keV to 85 keV, i.e., 1000 km/s to 4000 km/s) using the SupraThermal Electrons and Protons (STEP) instrument. As shown in the second panel of Fig. 4, STEP sees a clear enhancement of suprathermal ions accelerated in the sheath region, and this is also confirmed by EPD's Electron Proton Telescope (EPT, not shown here), which saw enhancements of ions up to 100 keV. No significant enhancements of energetic electrons were observed in EPT or STEP.

The flux rope is followed by a separate structure with enhanced levels of magnetic turbulence. In comparison with the solar wind plasma observations near Earth (see Fig. 5 and its description later in this section), where clear increases in solar wind

speed and temperature are observed, we identified this to be a stream interaction region (SIR), followed by a stream of high-speed solar wind. We determined the onset times of the three SIR structures, the forward shock (F), stream interface (I), and reverse shock (R) at SolO by searching for shock signatures in the magnetic field data that are similar to those seen at Wind, although the identification is less reliable than at Earth due to the missing SWA data. In addition, STEP and EPT see another enhancement of energetic ions close to the stream interface.

However, the main focus of this study is the signature in the high energy particles, where a clear Forbush decrease with a drop amplitude of around 3 % in both the GCR channel as well as the C detector counters is observed (bottom panels of Fig. 4). The C counter is plotted in ten-minute time averages, with an additional curve showing a smoothed version of these data (rolling mean) and the GCR channel is shown in a similar fashion with a one-hour cadence. Due to the higher count rate, the FD is especially well observed in the C counters. The main part of the decrease occurs during the passage of the flux rope — the decrease within the sheath region is well below 1 %. This means that the assumption of the ForbMod model (Sect. 3) that only the flux rope effect is taken into account is fulfilled. A second GCR decrease is observed after the CME, coinciding with the passage of the SIR.

Figure 5 shows the in situ measurements of the CME arrival near Earth, including solar wind magnetic field and plasma data from the Magnetic Field Investigation (MFI, Lepping et al. 1995) and the Solar Wind Experiment (SWE, Ogilvie et al. 1995) on board the Wind spacecraft, as well as GCR measurements from the South Pole neutron monitor (SoPo), the GSM outputs and the CRaTER D2 counter. The measured speed of the CME at Wind is very slow, with a maximum of 370 km/s. The Wind and CRaTER measurements were shifted forward in time taking into account the radial distance to Earth (1 h 7 min for Wind at L1, and 15 min for CRaTER at the Moon; cf. inset in Fig. 1). These time shifts were calculated using the abovementioned maximum speed of 370 km/s, which is seen at the front of the CME flux rope. Considering this time shift, the shock arrival time at Earth is 02:40 UTC on April 20, and the flux rope arrived a few hours later at 09:01 UTC. In comparison to Solar Orbiter, the magnetic field strength of the flux rope has decreased to a maximum of  $B_{\text{max}} = 16.2$  nT, while the sheath region still has field intensities similar to the SolO measurement around 6 nT. Apart from the lower intensity, the magnetic field signatures of the flux rope look very similar to those observed at Solar Orbiter, showing the same south-east-north orientation. The large negative out-of-ecliptic component ( $B_z$ , or  $B_N$ ) seen at the beginning of the flux rope is a feature which is typically associated with high geoeffectiveness (e.g., Gopalswamy 2008). The sheath duration increased by more than two hours ( $\sim 60$  %), which is probably related to the accumulation of additional solar wind plasma in front of the CME as well as expansion due to the increasing velocity profile of the sheath region (see e.g., Manchester et al. 2005; Siscoe & Odstrcil 2008; Janvier et al. 2019; Freiherr von Forstner et al. 2020), while the expansion of the flux rope is more moderate at a bit over one hour ( $\sim 8$  %). The transit times from Solar Orbiter to L1 correspond to an average transit speed of 363 km/s for the flux rope front, which matches the in situ measured front speed of 370 km/s very well.

As mentioned earlier in this section, the SIR following the CME is clearly seen in the in situ data at Wind, showing signatures such as the increases in temperature and velocity as well as a decrease in density. According to these signatures, the time of the forward shock (F), stream interface (I), and reverse shock

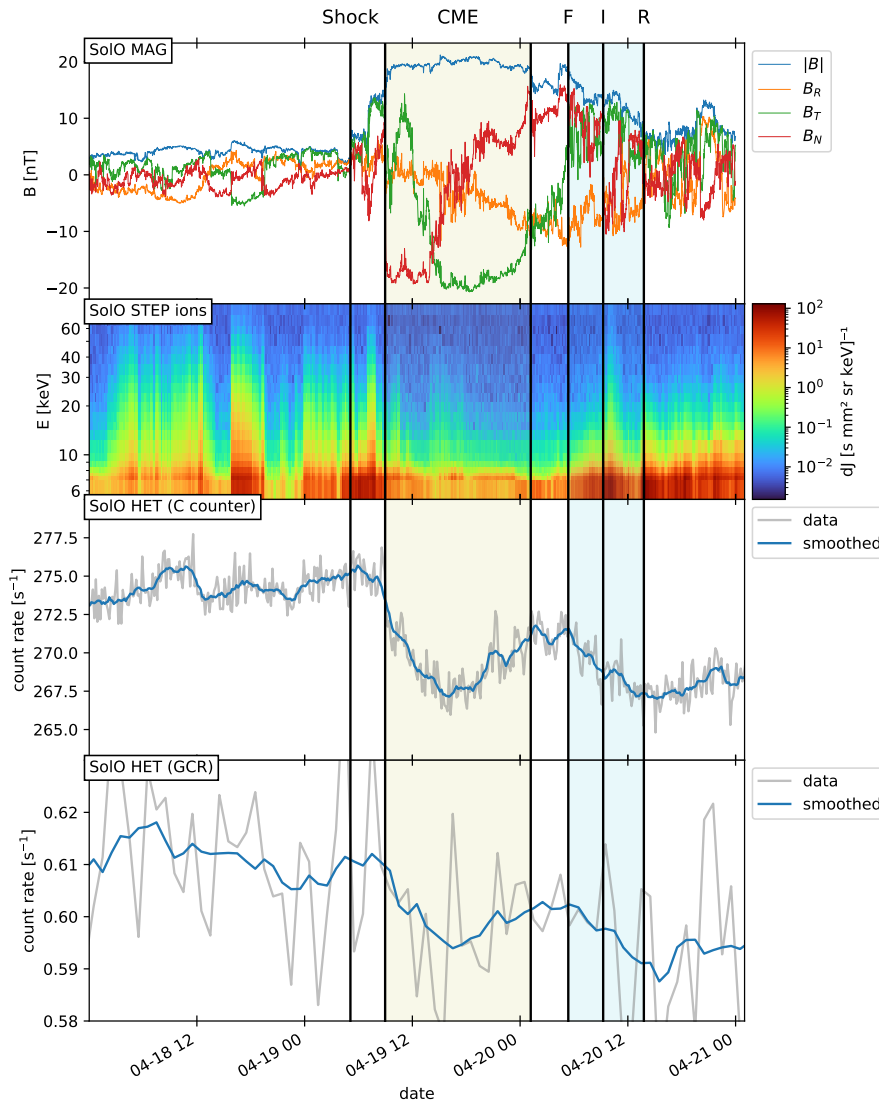


**Fig. 4.** Measurements from MAG, STEP, and HET on Solar Orbiter, showing the magnetic structure of the CME, suprathermal particle signatures, and the associated FD observations in the GCR channel and the C detector counter of HET. The MAG measurements are displayed in radial (R), tangential (T) and normal (N) coordinates. Black vertical lines and shaded regions mark the time periods corresponding to different events: Shock arrival, CME (flux rope) start and end, as well as forward shock (F), stream interface (I), and reverse shock (R) of the SIR.

(R) were marked in Fig. 5. Even though the solar wind plasma data are not available at Solar Orbiter for this event (as described above), it is clear from the magnetic field measurements that the SIR followed closely behind the CME at both locations, separated by a region of high plasma density (seen in the Wind measurements). Assuming an average solar wind speed within the SIR of approximately 400 km/s, the separation of the Parker spiral footpoints of SoLO and Earth is  $16.7^\circ$ , corresponding to an expected SIR delay time of 27.2 hours. The measured delay varies between 24.9 hours for the forward shock, 27.7 hours for the stream interface, and 31.4 hours for the reverse shock, suggesting that the SIR has significantly expanded in both directions. This means that the SIR may have affected the evolution of the CME, for example, by compressing it from behind. We will discuss this further in Sect. 5.

Comparing the GCR measurements at SoPo and CRaTER, as well as the outputs of GSM, when utilizing measurements of  $\sim 35$  neutron monitors, it can be seen that the relative amplitudes of the FD profiles induced by the CME at SoPo and from GSM are quite similar, whereas both are quite different compared to CRaTER. As discussed in Sect. 2.2, CRaTER covers a similar energy range as the HET C counter at SoLO, while neutron monitors have a larger cutoff energy. The South Pole neutron mon-

itor has much higher counting statistics than CRaTER, but the FD there only reaches an amplitude of 1.2 %, as higher energy particles are modulated less by the CME's magnetic field. This is also true for the outputs of GSM that reach an amplitude of 1.1 %. The minimum of the FD appears to fall within the magnetic cloud (MC), and as at SoLO, the MC seems to be the main driver of the FD in comparison to the shock-sheath structure, during which only a small decrease is observed. On the other hand, the FD at CRaTER has an amplitude of 2.0 %. The FD onset at CRaTER appears to be slightly earlier than the arrival of the flux rope, but the difference is only less than one orbital period of CRaTER, so this may also be an artifact of the altitude correction (cf. Sect. 2.2). The slightly enhanced periodic variations of the CRaTER signal seen close to the minimum of the FD are also a sign that the altitude correction is not completely suppressing the periodic signal due to the modulated GCR spectrum.

Figure 6 presents the density variations of cosmic rays at Earth obtained from GSM: A0 (in %), together with the components of the anisotropy  $A_{xy}$  (equatorial components) and  $A_z$  (polar component). The characteristics of the cosmic ray anisotropy that signify the effect of a MC on GCRs are summarized as follows: (a) the amplitude of  $A_{xy}$  is higher within the MC, reaching

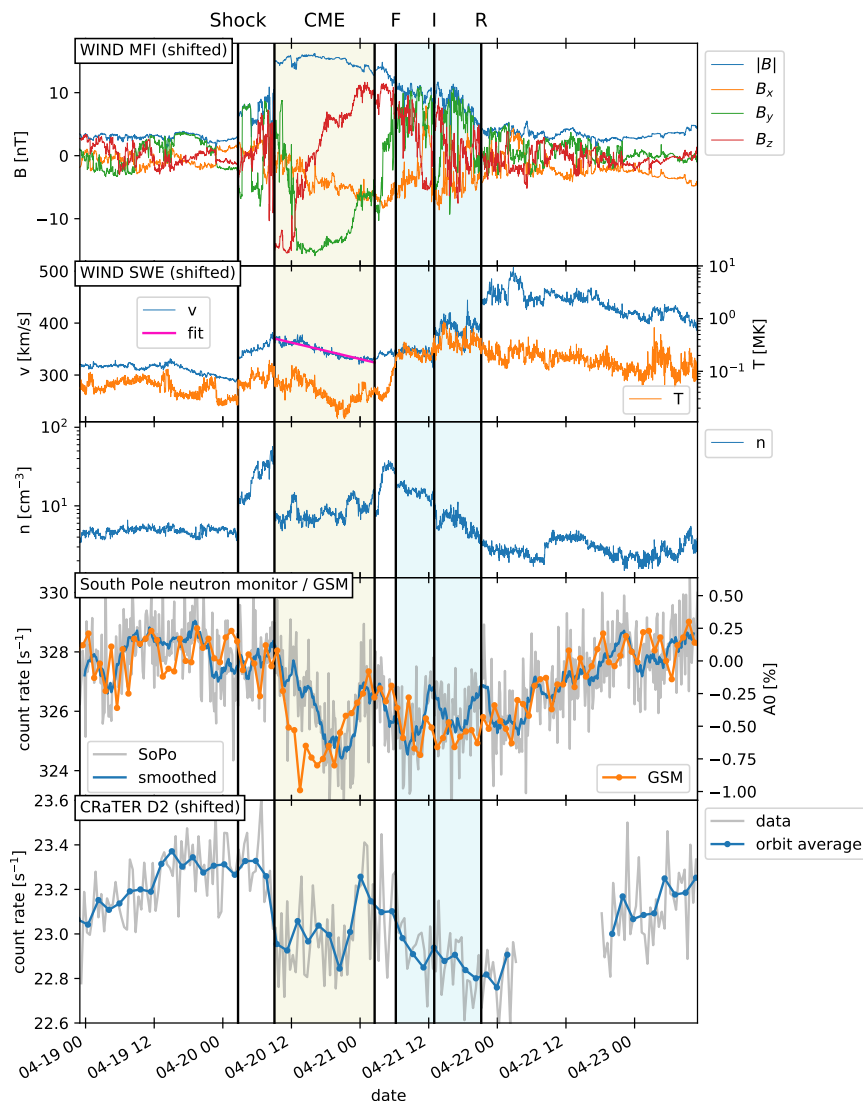


**Fig. 5.** Measurements near Earth from MFI and SWE on Wind and neutron monitors on Earth as well as the CRaTER D2 counter, showing the in situ signatures of the CME and the associated FD, as well as a high speed stream following afterwards. Wind data were shifted forward in time by 1 hour and 7 minutes to account for the expected transit time between the L1 Lagrange point and Earth, and CRaTER data were shifted by 15 minutes, corresponding to the Moon–Earth radial distance. Black vertical lines and shaded regions mark the time periods corresponding to different events: shock arrival, CME start and end, as well as forward shock (F), stream interface (I), and reverse shock (R) of the SIR. Wind MFI measurements are given in Heliocentric Earth Ecliptic (HEE) coordinates, with X pointing from the Sun to Earth and Z being perpendicular to the ecliptic pointing north, and Y completing the right handed triad. The general orientation of HEE is thus comparable to RTN, which is used for SoLo data in Fig. 4, and the difference to RTN is small. A linear fit to the velocity profile of the flux rope, which is used to determine the expansion speed as explained by Gulisano et al. (2012), is shown in pink. The second panel from the bottom shows both measurements from the south pole neutron monitor (gray, blue) and the GCR density variation at 10 GV (corresponding to 9.1 GeV proton energy) obtained from GSM.

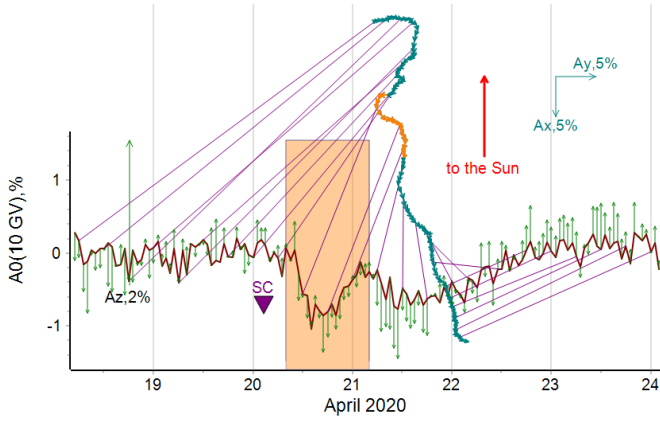
a maximum of  $\sim 1\%$  coinciding with the minimum of the FD; (b) the direction of the anisotropy vector (i.e., orange part of the vector diagram) changes abruptly when entering the MC (Belov et al. 2015); (c) there is a rotation of the  $A_{xy}$  vector within the MC; and (d) the north-south component  $A_z$  changes by  $1.1\%$  during the FD, including a reversal of direction during the decay phase of the FD (Abunin et al. 2013; Belov et al. 2015). The CME parameters calculated from the in situ data at Solar Orbiter and near Earth, as well as the onset times of the SIR structures are summarized in Table 1.

Figure 7 (also available as an online animation) shows the results from an application of the semi-empirical 3DCORE model (Möstl et al. 2018; Weiss et al. 2020), based on the SoLo MAG observations of the flux rope. This model provides a global context for the flux rope structure, propagation, and orientation at Solar Orbiter and Wind. Further applications of this model and its results are described in more detail by Davies et al. (2021), whereas here we show a few main results relevant for our study. In order to reconstruct the magnetic field configuration and its 3D structure, the 3DCORE model ensembles were fitted to an interval of the MAG data with a clean magnetic field rotation; here, we have a run that represents a best fit which covers an interval from Apr 19 11:13 UTC to Apr 20 01:59 UTC. This

interval starts about 2 hours later than the start of the flux rope interval stated above at 08:58 UT as the  $B_T$  component is positive for a short while after 09:00 UT, which is inconsistent with its unipolar excursion to  $B_T < 0$  later. This first feature in  $B_T$  cannot be fitted with the 3DCORE flux rope model, and thus we choose to narrow the fitting interval to what Davies et al. (2021) call the “unperturbed” inner part of the flux rope.

The 3DCORE technique consists of a Gold-Hoyle uniform twist magnetic field in an elliptical flux rope cross section placed in a 3D toroidal shape (Weiss et al. 2020). Here, we set the cross section aspect ratio, otherwise a free parameter to be determined from the fitting analysis, to a value of 2.0, which is consistent with the angular width of the CME void in Heliospheric Imager observations (Davies et al. 2021). In Fig. 7a-c, a 3D visualization of the 3DCORE envelope is presented from several viewpoints at the time of the Forbush decrease onset at Earth. Fig. 7d demonstrates the ability of the model to fit the Solar Orbiter observations. In Fig. 7e, we propagated the model to the Wind spacecraft self-similarly, where the power law exponents for the expansion of the diameter and magnetic field (as defined in Equation 2) were set to previously empirically derived values of  $n_a = 1.14$  and  $n_B = 1.64$ , respectively. Those values are based on a power law fit of the mean total magnetic field of a large sample of in





**Fig. 6.** GCR density variation  $A_0$  at Earth obtained from GSM at a fixed rigidity of 10 GV (brown line, corresponding to 9.1 GeV proton energy), together with the first harmonic of the cosmic ray anisotropy. The equatorial component  $A_{xy}$  of the anisotropy is displayed as a vector diagram (teal and orange triangles), which are connected to the corresponding points in time on the  $A_0$  plot with magenta lines. Additionally, the north-south component  $A_z$  is shown as green vertical arrows on top of  $A_0$  time profile. The shaded rectangle and the orange part of the vector diagram correspond to the duration of the magnetic cloud (MC). The shock arrival at Earth is indicated by the arrow labeled SC (“sudden storm commencement”), and the direction to the Sun in the vector diagram is indicated with a red arrow. The components of the anisotropy  $A_x$  and  $A_y$  that define the plane for the calculation of  $A_{xy}$  are indicated on the top right corner of the figure. Numbers at each anisotropy component on the figure indicate the scale used for the plotting of the relevant arrows.

situ measured CME flux ropes in the inner heliosphere (Leitner et al. 2007).

The 3DCORE torus propagates according to a drag-based model (see details in Weiss et al. 2020). The results show that the modeled magnetic field components are consistent at Solar Orbiter and Wind at L1, but as seen in Fig. 7e, there is a time shift between the model and the observations of the flux rope magnetic field at Wind (concerning all components and the total field). This points to a slight inconsistency of the Solar Orbiter fit results when they are propagated to L1, which most likely arises from the shape and direction of the 3DCORE torus being determined with data from a single spacecraft, and it is expected that due to the model assumptions this does not exactly reproduce the observations at another spacecraft. This inconsistency can be alleviated with simultaneously fitting 3DCORE to Solar Orbiter and Wind in situ magnetic field data, but this is the subject of future studies.

In Fig. 7, we show a model which uses parameters representative of the best fit, but the fitting algorithm that we use (Weiss et al. 2020) allows us to derive distributions for each of the flux rope parameters. The main results from the Solar Orbiter 3DCORE fit (with the results stated as means  $\pm$  standard deviations) are as follows: the CME is directed at  $(13 \pm 5)^\circ$  longitude (HEEQ) and  $(-5 \pm 5)^\circ$  latitude, which means that it has a close to central impact at Solar Orbiter and Wind and the observations at the two spacecraft are clearly connected. The orientation of the axis is  $(11 \pm 13)^\circ$  to the solar equatorial plane, thus, it is a low inclination flux rope. At the heliocentric distance of Wind (0.995 AU), the axial magnetic field strength in the model is  $(14.3 \pm 0.9)$  nT, and the model flux rope has a diameter of  $(0.114 \pm 0.022)$  AU. For Solar Orbiter at 0.809 AU, this axial field is  $(20.1 \pm 1.2)$  nT and the diameter is  $(0.090 \pm 0.017)$  AU.

**Table 1.** CME and SIR parameters derived from the in situ measurements at Solar Orbiter and near Earth.

	Solar Orbiter	near Earth
Radial distance		
$R$ [AU]	0.809	0.995 <sup>a</sup> / 1.005 <sup>b</sup>
CME and SIR onset times		
$t_{\text{shock}}$ [UTC]	2020-04-19 05:06	2020-04-20 02:40
$t_{\text{CME}}$ [UTC]	2020-04-19 08:58	2020-04-20 09:01
$t_{\text{CME end}}$ [UTC]	2020-04-20 01:11	2020-04-21 02:32
$t_{\text{forward shock}}$ [UTC]	2020-04-20 05:22 <sup>c</sup>	2020-04-21 06:15
$t_{\text{stream interface}}$ [UTC]	2020-04-20 09:15 <sup>c</sup>	2020-04-21 12:58
$t_{\text{reverse shock}}$ [UTC]	2020-04-20 13:47 <sup>c</sup>	2020-04-21 21:11
Duration		
$\Delta t_{\text{sheath}}$ [h]	3.9	6.4
$\Delta t_{\text{CME}}$ [h]	16.2	17.5
In situ parameters		
$B_{\text{max}}$ [nT]	21.2	16.2
$\bar{v}_{\text{CME}}$ [km/s]	—	347
$v_{\text{exp}}$ [km/s]	—	46
$A_{\text{FD}}$ [%]	2.9	2.0

**Notes.** Listed Forbush decrease amplitudes  $A_{\text{FD}}$  correspond to the HET C counter at Solar Orbiter and the CRaTER D2 counter near Earth.

<sup>(a)</sup> L1 <sup>(b)</sup> Earth <sup>(c)</sup> Due to the missing plasma data, SIR onset times are less certain at SolO.

As explained by Démoulin & Dasso (2009) and Gulisano et al. (2012), the measured velocity profile of the flux rope can be used to estimate the expansion factor,  $n_a$ , which describes the increase in the flux rope radius  $a$  with the radial distance from the Sun (see definition in Sect. 3). From a linear fit, we calculate the expansion speed  $v_{\text{exp}}$ , which is the velocity difference between the front and rear end of the flux rope, to be 46 km/s, and together with the mean speed of  $\bar{v}_{\text{CME}} = 347$  km/s, we calculate:

$$n_{a, \text{in situ @ Wind}} = \frac{v_{\text{exp}}}{\Delta t_{\text{CME}}} \frac{R}{\bar{v}_{\text{CME}}^2} = 0.90, \quad (6)$$

where  $R$  is the radial distance of Wind at this time (see Eq. 1).

It is also possible to calculate a value of  $n_a$  for the propagation between SolO and Wind, using the two in situ measurements:

$$n_{a, \text{SolO-Wind}} = \log \left( \frac{\Delta t_{\text{CME, Wind}}}{\Delta t_{\text{CME, SolO}}} \right) / \log \left( \frac{R_{\text{Wind}}}{R_{\text{SolO}}} \right) = 0.37, \quad (7)$$

and, similarly, we can derive the expansion factor  $n_B$  for the magnetic field magnitude between SolO and Wind:

$$n_{B, \text{SolO-Wind}} = -\log \left( \frac{B_{\text{max, Wind}}}{B_{\text{max, SolO}}} \right) / \log \left( \frac{R_{\text{Wind}}}{R_{\text{SolO}}} \right) = 1.30, \quad (8)$$

The values for both  $n_{B, \text{SolO-Wind}}$  and  $n_{a, \text{in situ @ Wind}}$  are within the typical ranges found in previous observational studies, as described in Sect. 3. The value of  $n_{a, \text{SolO-Wind}}$  is unusually low and quite different from the in situ measurement. This could be interpreted as a sudden change in the expansion rate of the CME, but may also be related to the difference of the inherent assumptions in the two methods; for example, the local determination of the expansion factor at Wind (Eq. 6) assumes a quasi-undisturbed

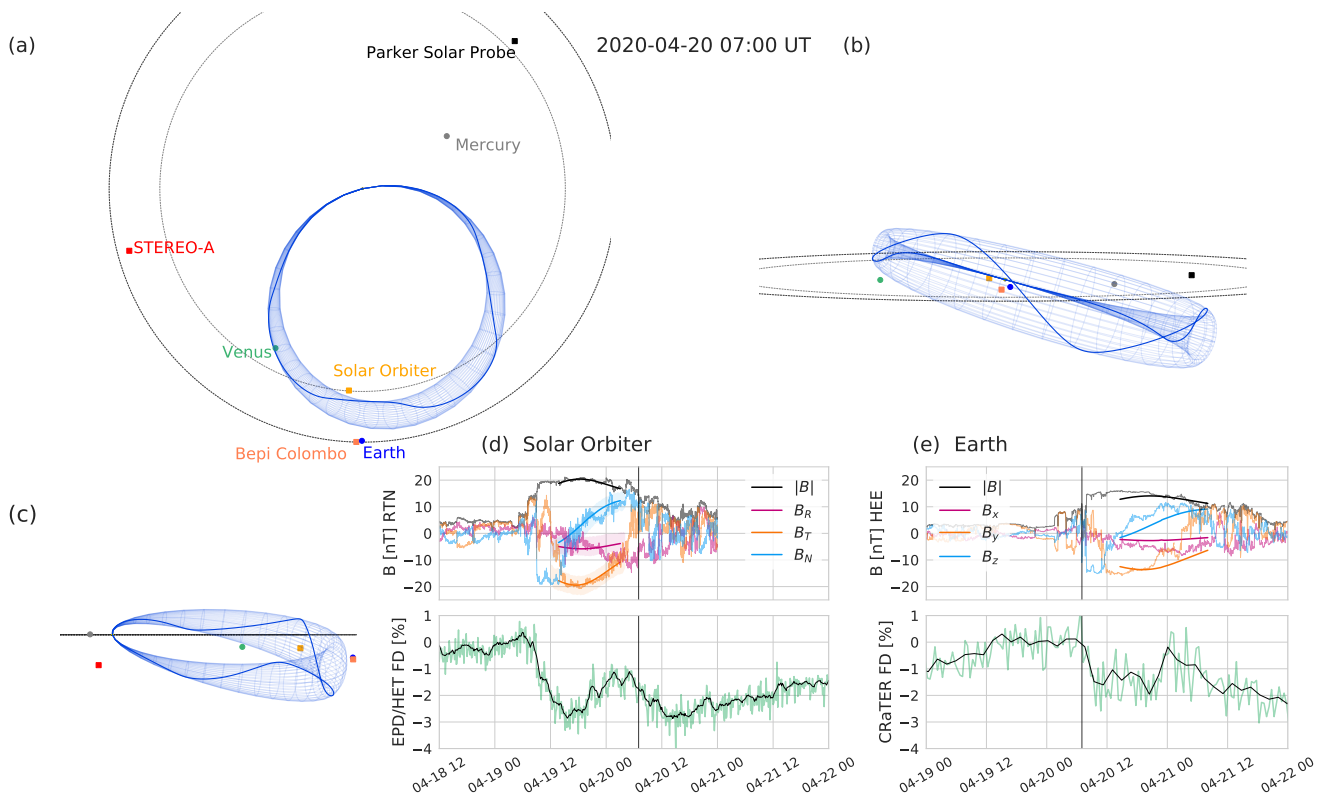


**Fig. 7.** Visualization of the results of the 3DCORE flux rope model fitted to the Solar Orbiter MAG observations, shown at the time of the onset of the Forbush decrease at Earth. The reconstructed 3D flux rope structure is shown: (a) looking down from the solar north pole onto the solar equatorial plane, (b) in a frontal view along the Sun–Earth line, and (c) in a side view at a 75 degree angle, the longitude of STEREO–A to Earth. A flux rope field line is highlighted as a solid blue line. The panels (d) and (e) show the in situ magnetic field data from Solar Orbiter and Wind at Earth/L1 compared to the GCR variation as a percentage drop in the amplitude measured by EPD/HET and CRaTER. The Wind magnetic field components are given here in Heliocentric Earth Ecliptic (HEE) coordinates, as in Fig. 5. The 3DCORE modeled magnetic field is overplotted in panel (d) and propagated to Earth as shown in (e). An animation of this figure is available as an **online movie**.

expansion of the CME following the current velocity profile within the flux rope, while external influences are not taken into account. In contrast, the observation of a SIR that follows closely behind the CME (as described above) suggests that there may have been some interaction between the two structures that may have affected the expansion. This is discussed in more detail in Sects. 4.3 and 5. We also note that the derived values of  $n_a$  and  $n_b$  are both lower than the fixed values assumed in the 3DCORE model, but this is partly due to the fact that the 3DCORE modeling excludes the first part of the flux rope duration (as explained above). Also, as stated above, a more detailed 3DCORE analysis fitting the CME structure simultaneously at both locations will be explored in future studies.

#### 4.2. Remote sensing observations

Due to its 75° longitudinal separation from Solar Orbiter and Earth at the time (cf. Fig. 1), the STEREO-A spacecraft has provided excellent remote-sensing observations of this CME event. Figure 8 shows observations from the Sun Earth Connection Coronal and Heliospheric Investigation suite on board STEREO-A (SECCHI, Howard et al. 2008), namely, the COR2 white-light coronagraph, as well as from the Heliospheric Imagers (HI). The COR2 image shows two CMEs launched from the Sun in close succession on April 14–15 2020. The CME visible on the right side of the COR2 image, which first appears at approximately 19:30 UTC on April 14 and then slowly moves outward, is the

one that headed towards SoLo and Earth, while the larger CME on the left side is backside from the Earth point of view.

To reconstruct the CME shape near the Sun, we applied the Graduated Cylindrical Shell model (GCS, Thernisien et al. 2006; Thernisien 2011) to the STEREO-A/COR2 and SOHO/LASCO C2, and C3 (Brueckner et al. 1995) coronagraph images, which allows us to derive such parameters as latitude and longitude as well as the flux rope height and radius. In the course of this study, we developed a new implementation of the GCS model in Python<sup>4</sup> and verified its results against the existing SolarSoft IDL version. During the reconstruction process, it became apparent that the structure seen on the east limb from SOHO/LASCO C3 cannot belong to the Earth-directed CME. To fit the GCS geometry to this structure, it would have been necessary to shift the CME longitude by more than 30° away from Earth or increase the flux rope height significantly, which contradicts the position of the clear flux rope structure observed at STEREO-A/COR2 and the in situ observation at Earth and Solar Orbiter. Considering this, we suspect that this signature is instead caused by the backside CME and we verified this assumption by also approximately fitting the backside CME with the GCS model (as plotted in orange in Fig. 8). The Earth-directed CME is not clearly seen in the LASCO C3 images, but it shows a weak signature in C2 on the northwestern limb. This structure was used in conjunction with the clear observations in the STEREO-A COR2 data to reconstruct the CME (plotted in blue in Fig. 8). The GCS results

<sup>4</sup> [https://github.com/johan12345/gcs\\_python](https://github.com/johan12345/gcs_python),  
<https://doi.org/10.5281/zenodo.4443203>

show that the two CMEs partly overlap in the SOHO/LASCO observations due to the line of sight effect, which is probably the reason why the Earth-directed CME is only seen from SOHO on the west limb. The fit parameters for both CMEs are listed in Table 2, where the uncertainties were derived by performing the GCS fit for the Earth-directed CME 40 times and then calculating the mean and standard deviation of each parameter. This was not done for the backside CME as its parameters are not needed for the further analysis in this study. The GCS fit results for the latitude, longitude, and tilt angle are also approximately consistent with the data derived from the 3DCORE reconstruction based on the in situ data (see Sect. 4.1, although these are, of course, also associated with some uncertainties. We note that the 40 GCS fits of the Earth-directed CME were performed by a single person, which may decrease the uncertainties compared to a result produced using independent reconstructions from different scientists. Still, care was taken to sample a large range of possible values for each parameter and adjust the remaining parameters accordingly to fit the coronagraph images. Additionally, the data were compared to a single independent GCS reconstruction by another researcher and the results agree within the given uncertainty ranges.

There is also no obvious signature of the CME in the low corona (low coronal signatures, LCS), as observed with the SDO/AIA (Lemen et al. 2012) 211 Å extreme ultraviolet (EUV) images, making it a challenge to identify the CME source region. A weak brightening is observed at approximately 2°N 8°E, but this is too far away from the GCS-reconstructed CME longitude of  $(18 \pm 7)^\circ$ W. Thus, the CME can be considered as a type of “stealth CME” (see e.g., Howard & Harrison 2013, and references therein) both due to the weak LCS and the lack of a clear halo CME in the coronagraphs from the Earth point of view. Stealth CMEs have weak LCS because only a relatively small amount of energy is released from the corona at their onset due to their low speed (typically  $< 300$  km/s according to Ma et al. (2010) and these signatures may be too weak to be detected with the established observational and data processing techniques (e.g., Alzate & Morgan 2017). A more detailed study of the source region of this CME will be performed by O’Kane et al. (2021, in preparation for A&A).

As a result of the GCS fit, we derived the initial height of the flux rope  $R_0 = (9.64 \pm 0.40) R_\odot$  and the initial radius at the apex  $a_0 = (1.93 \pm 0.15) R_\odot$ , calculated using the equation from Thernisien (2011). These parameters will be needed for the application of the ForbMod model in Sect. 4.3.

Based on the GCS results, we can make a new calculation for the expansion factor  $n_a$ : The calculation in Equation 6 corresponds to the instantaneous expansion of the flux rope near 1 AU, which may not be the same as closer to the Sun. The average expansion factor between the Sun and Earth can be calculated by comparing the initial flux rope size  $a_0$  with the one measured in situ at Wind:

$$n_{a,\text{Sun-Wind}} = \log\left(\frac{a_{\text{Wind}}}{a_0}\right) / \log\left(\frac{R_{\text{Wind}}}{R_0}\right) = 0.70, \quad (9)$$

where  $R_{\text{Wind}}$  is the radial distance of the Wind spacecraft from the Sun and  $a_{\text{Wind}} = \Delta t_{\text{CME}} \cdot \bar{v}_{\text{CME}}/2 = 15.7 R_\odot$  is the flux rope radius calculated from the in situ data (see Table 1). A similar value of  $n_a = 0.69$  can be calculated from the SoLo measurements, when assuming the CME speed to be the same as at Wind.

STEREO-A HI observations clearly show the CME signature out to elongation angles of approximately 35° (corresponding to a radial distance of  $\sim 0.6$  AU), as seen in the running dif-

**Table 2.** Results from the graduated cylindrical shell (GCS) model.

	CME 1 <sup>a</sup>	CME 2 <sup>b</sup>
HEEQ Longitude [°]	18 ± 7	229
HEEQ Latitude [°]	3 ± 3	−1
Tilt angle [°]	18 ± 6	6
Half angle [°]	35 ± 11	15
Height [ $R_\odot$ ]	9.5 ± 0.8	14.73
Ratio $\kappa$	0.23 ± 0.04	0.30
FR radius at apex [ $R_\odot$ ]	1.8 ± 0.3	3.78

**Notes.** A GCS fitting was applied in the 2020-04-15 05:39:00 UTC image from STEREO-A COR2 and the 2020-04-15 05:36:07 UTC image from SOHO/LASCO C2. Results are plotted in Fig. 8. Error bars are given only for CME 1, as CME 2 is not further studied here.

<sup>(a)</sup> Directed towards SoLo and Earth <sup>(b)</sup> Backsided as seen from SoLo/Earth

ference images and the time-elongation map (Fig. 8, bottom panels). This event is cataloged by the HELCATS project<sup>5</sup> under the ID HCME\_A\_20200415\_01. According to the self-similar expansion fitting (SSEF) result (Davies et al. 2012) given in the HELCATS HIGeoCat catalog (Barnes et al. 2019), the CME direction in Heliocentric Earth Equatorial (HEEQ) coordinates is  $-6^\circ$  in longitude and  $-2^\circ$  in latitude. The longitude does not match what we determined in our GCS reconstruction (Table 2), but as the SSEF technique only uses data from a single spacecraft and makes certain assumptions about the CME, such as a constant speed and a fixed half-width of 30°, it is known to often produce large uncertainties for the CME longitude (see e.g., Barnes et al. 2019). The SSEF results can also be used to calculate the arrival time at Solar Orbiter and Earth, as described by Möstl et al. (2017). The calculated arrival times available from the ARRCAT v2.0<sup>6</sup> are 2020-04-19 09:10 ± 3.2 h for SoLo and 2020-04-20 09:45 ± 4.0 h for L1, which are both about eight hours later than the in situ shock arrival times. This is well within a usual range of arrival time errors with this method of ±17 hours. (Möstl et al. 2017). The arrival speed at Earth is predicted as  $(335 \pm 11)$  km/s, which is also consistent with the in situ measured CME speed (mean speed  $\bar{v} = 347$  km/s, see Table 1).

#### 4.3. Application of the ForbMod model

In the previous sections (Sects. 4.1 and 4.2), we show how we derived all input parameters necessary for applying the ForbMod model to the Forbush decreases at Solar Orbiter and Earth. For the flux rope radius expansion factor,  $n_a$ , multiple values were calculated from measurements at different locations, with quite significant differences:  $n_{a,\text{SoLo-Wind}} = 0.37$ ,  $n_{a,\text{in situ @ Wind}} = 0.90$ , and  $n_{a,\text{Sun-Wind}} = 0.70$ . Additionally, we derived one value of the magnetic field expansion factor  $n_{B,\text{SoLo-Wind}} = 1.30$ , based on the SoLo and Wind in situ measurements of the magnetic field.

While  $n_B$  is also used separately to derive the radial dependence of the diffusion coefficient  $D$ , the key purpose of the two expansion factors within ForbMod is to calculate the so-called expansion type, a quantity defined as  $x = n_B - 2n_a$  (see Eq. 4). Consequently, the model is very sensitive to the values of  $n_a$  and  $n_B$ .  $x$  describes the evolution of the magnetic flux and

<sup>5</sup> <https://www.helcats-fp7.eu/>

<sup>6</sup> <https://helioforecast.space/arrcat>,  
<https://doi.org/10.6084/m9.figshare.12271292>



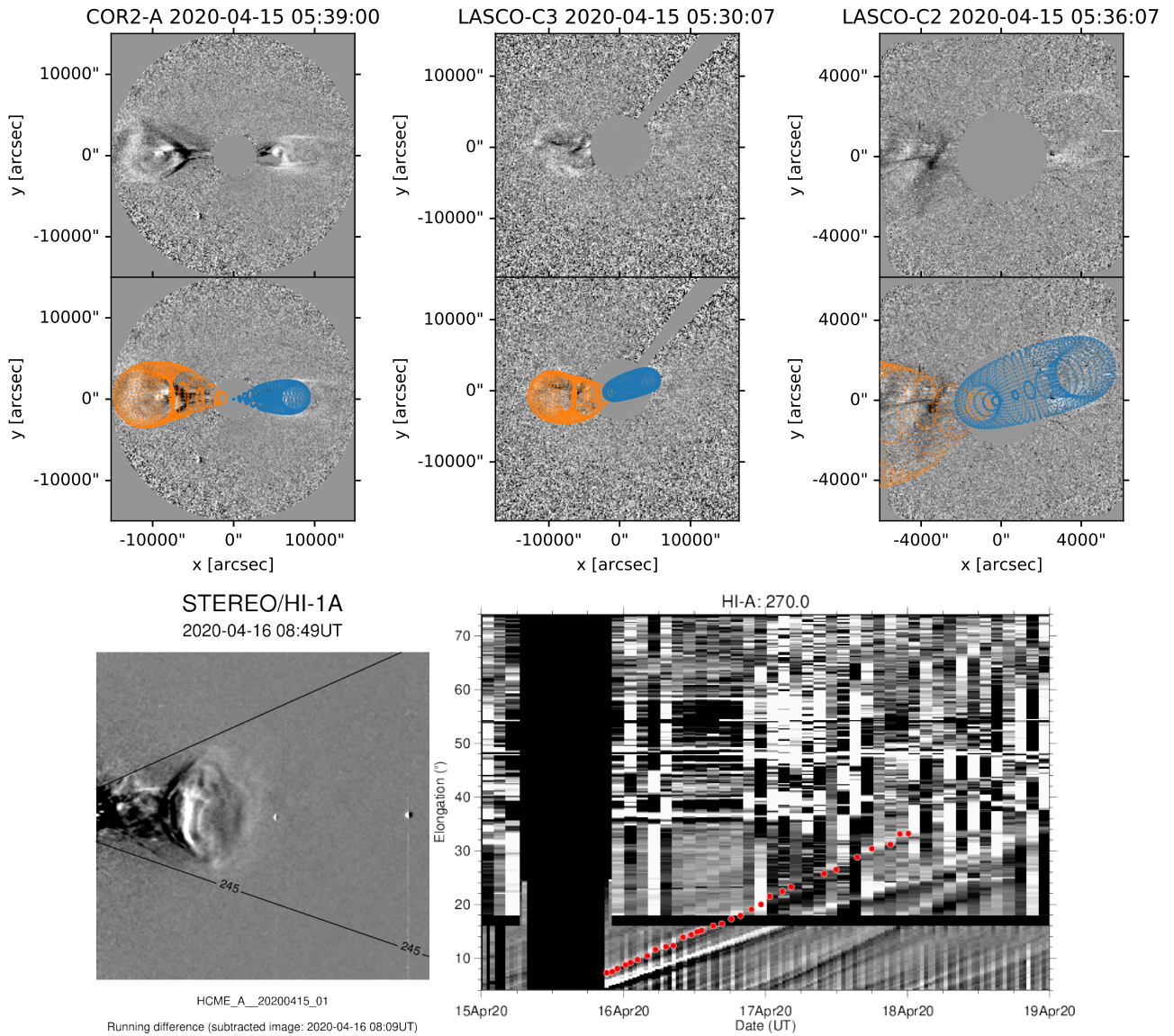


**Fig. 8.** Remote sensing observations of the CME. In the STEREO-A COR2 and SOHO LASCO C2 and C3 running difference images (top part), the GCS fitting was applied to derive the parameters  $R_0$  and  $a_0$  for the ForbMod model (see results in Table 2). The blue markings denote the Earth-directed CME we are investigating, while the CME fitted in orange is backside and launched a few hours earlier. STEREO-A HI observations (bottom left) and time-elongation maps (bottom right) are provided by the HELCATS project.

is assumed to be constant over the course of the CME propagation, that is, the magnetic flux increases or decreases at the same rate. Thus, the inconsistency of the measured  $n_a$  values suggests that  $n_B$  must also have changed to keep  $x$  constant. So, we can derive  $x = n_{B,\text{Solo-Wind}} - 2n_{a,\text{Solo-Wind}} = 0.55$ , and then, under the assumption that  $x = \text{const.}$ , calculate a corresponding  $n_B$  for each of the measured  $n_a$  values. The results of this calculation are listed in Table 4. Of course, in the case of this event,  $x = \text{const.}$  is a quite bold assumption to make considering the observed variation of  $n_a$ , but due to the lack of additional observations of  $n_B$ , there is no other way to derive the necessary input parameters from observations. We will discuss the possible implications of this in more detail in Sect. 5.

To summarize, we list all the parameters that are used for the application of ForbMod again in Table 3. We ran ForbMod for each of the  $n_a$  and  $n_B$  pairs that we calculated (Table 4), as well as for a “best fit” result reproducing the measured FD amplitudes at Solar Orbiter HET and CRaTER. Apart from the

response functions, transit times and radial distances, the ForbMod input parameters were always the same for both locations. It also must be noted that following the observed variation of  $n_a$ , the duration of the FD profile calculated with ForbMod was not derived from the  $a(r)$  power law assumed by ForbMod (equation 2), but instead was fixed to the observed flux rope duration. The ForbMod best fit was obtained by calculating the FD amplitudes across the whole reasonable parameter space of  $n_a$  and  $n_B$  (while keeping all other parameters fixed) and then selecting the set of parameters that produced the lowest sum of squared residuals with respect to the two in situ measured amplitudes at HET and CRaTER (see Table 1).

The ForbMod results for the “best fit” parameters are shown in Fig. 9, where the time profile calculated using Equation 5 is plotted in red and the measurements in blue and gray (as previously shown in Figures 4 and 5). It can be seen that for these parameters, there is a good agreement between the model and observations: ForbMod aptly describes the relatively symmet-

**Table 3.** Input parameters for the ForbMod model

Parameter	Source	Section	Value
GCR spectrum	Force-field approximation, Gieseler et al. (2017)	3	$\Phi$ for June 2009
Diffusion coefficient $D$	Empirical function from Potgieter (2013) with parameters from Potgieter et al. (2014)	3	parameters for 2009
Detector response function	Geant4 simulation results	2.1, 2.2	See Fig. 3
Magnetic field $B_c$	$B_{\max}$ in Wind data	4.1	$B_c = 16.2$ nT
expansion factors $n_a, n_B$	Calculation assuming $x = \text{const.}$ (Eq. 4) / best fit	4.3	see Table 4
Flux rope parameters $R_0, a_0$	GCS reconstruction	4.2	$R_0 = 9.64 R_\odot$ , $a_0 = 1.93 R_\odot$
Diffusion time ( $\approx$ transit time)	In situ arrival time, Launch time: time of GCS fit	4.1, 4.2	$t_{\text{SolO}} = 99$ h, $t_{\text{Earth}} = 123$ h
Velocity profile	linear fit to in situ measurements at Wind	4.1	see Table 1

**Table 4.** Pairs of expansion factors  $n_a, n_B$  used for the ForbMod model, and resulting FD amplitudes at SolO HET, CRaTER and the South Pole neutron monitor.

Calculation	Sun $\rightarrow$ Wind	SolO $\rightarrow$ Wind	in situ @ Wind	best fit <sup>a</sup>
$n_a$	0.70	0.37	0.90	1.08
$n_B$	1.95 <sup>b</sup>	1.30	2.36 <sup>b</sup>	2.01
$x^c$	0.55	0.55	0.55	-0.15
$A_{\text{FD, SolO}} [\%]$	< 0.01	< 0.01	1.25	2.90
$A_{\text{FD, CRaTER}} [\%]$	< 0.01	< 0.01	0.50	2.00
$A_{\text{FD, SoPo}} [\%]$	< 0.01	< 0.01	0.03	0.44

**Notes.** Each column in the table corresponds to one set of input parameters  $n_a$  and  $n_B$  that was used with ForbMod. The modeled FD amplitude for the GSM data (10 GV) is < 0.01 % for all four sets of input parameters and not shown here.

<sup>(a)</sup> Best fit was obtained by constraining the FD amplitudes at SolO and CRaTER. <sup>(b)</sup> These quantities were calculated assuming that  $x = 0.55$  (see discussion in Sect. 4.3).

<sup>(c)</sup> Calculated using Eq. 4.

ric Forbush decrease caused by the flux rope CME and reproduces the observed FD amplitudes. Of course, the second decrease caused by the SIR is not included in the model, which explains the obvious deviation of the measurements from the model after the flux rope passage. The effect of the spacecraft model included in the HET response function (see Sect. 2.1) is significant, applying ForbMod using the response function without the spacecraft would lead to a  $\sim 20$  % larger FD (amplitude of 3.52 %, not shown here).

For the other parameters,  $n_a$  and  $n_B$ , derived from the observations, ForbMod results for the FD amplitude at SolO and CRaTER are shown in Table 4. With all these parameter sets, it can be seen that ForbMod underestimates the amplitude of the FD. The closest result is obtained using the in situ parameters

measured at Wind, but even in this case the modeled FD amplitude is less than half of the measurement. For the other sets of parameters, ForbMod predicts the flux rope to already be completely filled with GCRs by the time it reaches SolO and Earth, so that the FD amplitude is < 0.01 %.

In addition to SolO HET and CRaTER, we applied ForbMod at Earth with different response functions to model the FDs observed at the South Pole neutron monitor (SoPo) and in the GSM data. For the latter, we applied ForbMod monoenergetically at the fixed rigidity of 10 GV (corresponding to 9.1 GeV proton energy) that is used by GSM, while for the former we assume a constant response above a cutoff energy of 450 MeV (see Sect. 2.3). With these results, both the FDs at SoPo and GSM data are significantly underestimated, with a maximum amplitude of 0.44 % for SoPo and well below 0.01 % for GSM in all cases. To obtain the observed FD amplitude on the order of 1 % from the model, especially for the higher energy of GSM, the parameters  $n_a$  or  $n_B$  (or both) would need to be increased even more, which is not supported by observations or the previous observational constraints cited in Sect. 3.

## 5. Discussion and conclusions

In this study, we present in situ and remote sensing observations of the first flux rope CME that hit the Solar Orbiter spacecraft on April 19 and Earth on April 20, 2020. Furthermore, we study the Forbush decrease that it caused at both SolO and near Earth. This event is considered to be a “stealth CME” as it showed only weak signatures from the point of view of Earth in the EUV observations of the low corona. Remote sensing observations of this CME were only possible thanks to the ideal position of the STEREO-A spacecraft, which could track the CME from the outer corona until  $\sim 0.6$  AU. At SolO and Earth, the CME was followed by a SIR, which is also clearly observed at both locations in the in situ magnetic field and cosmic ray signatures.

The largest FDs in terms of magnitude often require the presence and combined effect of the shock-sheath region and the following ejecta, both of which are necessary for deep GCR depressions (e.g., Papaioannou et al. 2020). Additionally, CMEs



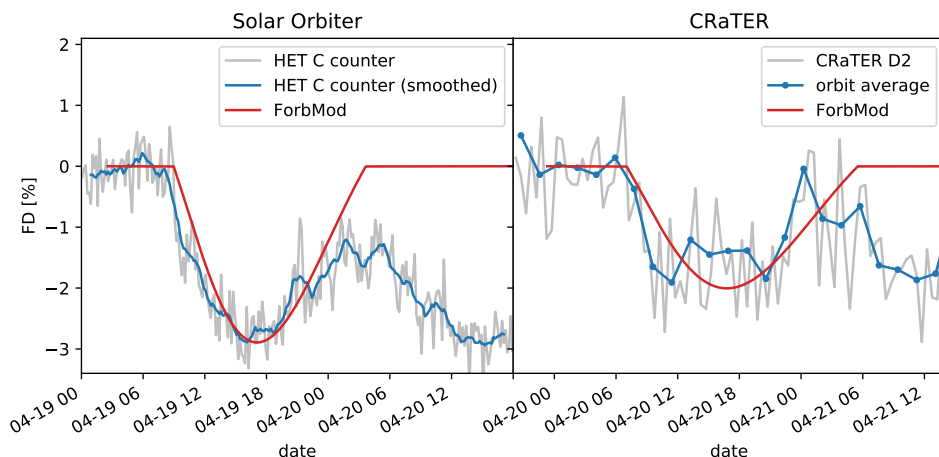


**Fig. 9.** ForbMod model results at Solar Orbiter and CRaTER, in comparison with the measured Forbush decreases at Solar Orbiter and CRaTER. The measurements are plotted in the same fashion as in Figures 4 and 5, but normalized to their pre-onset values to reflect the relative variation of the GCR count rate. Input parameters for ForbMod are listed in Tables 3 and 4. Also,  $n_a$  and  $n_B$  were used from the “best fit” result.

that are characterized as magnetic clouds (MCs) are more often associated with large FDs (Richardson & Cane 2011). However, although the CME studied in this work was associated with a shock and a clear MC observed at both SoLo and Earth, the resulting amplitude of the FD at Earth was relatively low, especially at higher GCR energies measured by neutron monitors and the GSM (only  $\sim 1\%$ ). This may lead to the assumption that only the flank of the CME hit SoLo and Earth, but this is not supported by the in situ flux rope modeling in Sect. 4.1 and the remote sensing observations presented in Sect. 4.2. Instead, the slow propagation speed of the CME below 350 km/s led to a very weak shock and an extremely long propagation time of more than five days from the Sun to Earth, which made it possible for GCRs to diffuse into the MC and thus decrease the observed FD amplitude. This explanation relates well to the concept of the ForbMod model because the diffusion of GCRs into the flux rope over time is the basis for its calculations. Based on the timing of the FD, it seems that the shock only had a very weak effect on the GCR modulation, with the majority having been caused by the MC.

Using input parameters derived from the CME observations, we applied the ForbMod model to reproduce the FDs observed by the SoLo HET C detector counter and the LRO CRaTER D2 counter. The derivation for most of the parameters was relatively straightforward. Only the expansion factors  $n_a$  and  $n_B$ , which describe the evolution of the flux rope radius and its magnetic field (which the model is quite sensitive to) could not be unambiguously determined from observations, as they seem to vary significantly depending on where and how they are measured. In addition, while  $n_a$  could be measured for different locations,  $n_B$  could only be measured based on SoLo and Wind observations (i.e., there is no measurement of  $n_B$  from the Sun to Earth). One set of parameters, derived assuming that the expansion type  $x$  is constant and using the  $n_a$  value measured in situ near Earth, only produces an FD amplitude of 1.29% at SoLo compared to the measurement of  $\sim 3\%$ . A “best fit” set of parameters  $n_a$  and  $n_B$ , which closely reproduce the FD amplitudes measured at CRaTER and HET, was also calculated, with an even higher value of  $n_a$ , that is, a stronger expansion of the flux rope size not supported by the observations, and a lower value of  $x$  closer to zero corresponding to a conserved magnetic flux (see Dumbović et al. 2018). In this case, the faster expansion (larger  $n_a$ ) counteracts the diffusion of GCRs into the flux rope, as described in Sect. 3, so that the FD amplitude becomes larger. However, even with the “best fit” parameter values, the higher-energy FD

measurements of the South Pole neutron monitor and the global survey method (GSM) could not be reproduced with ForbMod.

Using the observation of the flux rope evolution from SoLo to Earth in ForbMod yields FDs which do not agree with the observations. In addition, ForbMod best fit parameters yield global flux rope Sun-to-Earth evolutionary parameters, which are far from the values derived based on in situ measurement comparison between SoLo and Earth. This might indicate that Sun-to-Earth evolution of this CME was different from the SoLo-to-Earth evolution. A similar event, a slow stealth CME followed by a high speed stream was studied by He et al. (2018). The authors showed that the CME was compressed by the fast solar wind behind it, which caused an enhanced magnetic field and thus an unexpectedly high geoeffectiveness, and the same may have happened for this event. The inconsistent measured values of  $n_a$ , which correspond to a slower expansion of the flux rope between the Sun and 1 AU than suggested by the in situ measured velocity profile, can be a result of such a compression, thus indicating that the expansion behavior of this very slow CME may have changed during its propagation time. For instance, at some point during its propagation, the CME may have been slightly compressed by the SIR and expanded more freely at other times. Consequently, the assumption of ForbMod that the flux rope radius and its magnetic field follow power laws with constant indices  $n_a$  and  $n_B$  and that the resulting expansion type  $x$ , which describes the evolution of the magnetic flux, is also constant may not be valid in this more complex case. This may well be the reason why the model is not able to reproduce the higher energy FD measurements, even with a set of input parameters that fits the lower energy measurements of HET and CRaTER.

Another possible explanation for this discrepancy is that the energy dependence of the ForbMod-modeled FD amplitude may simply be overestimated for this event, resulting in too low FD amplitudes at higher energies. The reason for this, for example, could be that the empirical input parameters for the GCR spectrum and the energy dependence of the diffusion coefficient do not match the actual conditions at this time. This is an interesting result and should be investigated in more detail in future studies. For instance, a statistical validation of ForbMod against the results of the GSM, which has already been applied to a large catalog of FDs, may be helpful for examining whether this is a systematic problem in the description of the energy dependence for these higher GCR energies or whether this disagreement is a specific attribute of this CME event due to its low speed, very

long propagation time, and possible influence of the following SIR.

This study highlights the capabilities of the instruments on board the Solar Orbiter spacecraft, such as the high counting statistics of the HET C detector capable of detecting Forbush decreases. In addition, it shows that coordinated observations with Solar Orbiter and other spacecraft will be extremely important for the better understanding of space weather in the inner heliosphere. Spacecraft close to the Sun, such as Solar Orbiter and Parker Solar Probe, can serve as an upstream monitor to provide valuable information and early warning about CMEs. The CME in this case study also serves as an excellent example for a “stealth CME” that was still geoeffective due to its strong magnetic field even though it was not clearly seen in remote sensing observations from the point of view of Earth. This again highlights that the monitoring of Earth-directed CMEs requires in situ and remote sensing measurements at additional locations, for example, at Solar Orbiter and Parker Solar Probe as well as from STEREO-A or a future L5 mission. As the trajectory of Solar Orbiter moves closer to the Sun in the coming years and solar activity increases with the commencement of the Solar Cycle 25, space weather events during conjunctions with Earth as well as other spacecraft will become more probable, which will provide further exciting science opportunities.

**Acknowledgements.** J. v. F. thanks L. Seimetz and N. Lundt for their assistance in simulating the HET detector response functions. Additionally, we thank M. D. Looper and J. Wilson from the CRaTER team for providing the response functions of their instrument and helpful suggestions about the analysis of the CRaTER data. J. G. is supported by the Strategic Priority Program of the Chinese Academy of Sciences (Grant No. XDB41000000 and XDA15017300), the National Natural Science Foundation of China (Grant No. 42074222) and the CNSA pre-research Project on Civil Aerospace Technologies (Grant No. D020104). M. D. acknowledges support by the EU H2020 Grant Agreement 824135 (SOLARNET) and the Croatian Science Foundation under the Project 7549 (MSOC). A. P. acknowledges support by the TRACER project (<http://members.noa.gr/atpapaio/tracer/>) funded by the National Observatory of Athens (NOA) (Project ID: 5063) and from NASA/LWS project NNH19ZDA001N-LWS. M. A. and A. B. (IZMIRAN) are supported by the Russian Science Foundation under grant 20-72-10023. C. M., A. J. W., J. H., T. A. and M. B. thank the Austrian Science Fund (FWF): P31521-N27, P31659-N27, P31265-N27. This work, as well as the development of EPD on Solar Orbiter were supported by the German Federal Ministry for Economic Affairs and Energy, the German Space Agency (Deutsches Zentrum für Luft- und Raumfahrt e.V., DLR) under grants 50OT0901, 50OT1202, 50OT1702, and 50OT2002, by ESA under contract number SOL.ASTR.CON.00004, the University of Kiel and the Land Schleswig-Holstein, as well as by the Spanish Ministerio de Ciencia, Innovación y Universidades under grants FEDER/MCIU Agencia Estatal de Investigación/Projects ESP2105-68266-R and ESP2017-88436-R. The Solar Orbiter magnetometer was funded by the UK Space Agency (grant ST/T001062/1). Solar Orbiter EPD and MAG data are available in the Solar Orbiter Archive at <http://soar.esac.esa.int/soar/>. We acknowledge the NMDB database (<http://www.nmdb.eu/>), funded under the European Union’s FP7 Programme (contract 213007), for providing data. The data from South Pole neutron monitor is provided by the University of Delaware with support from the U.S. National Science Foundation under grant ANT-0838839. LRO/CRaTER Level 2 data are archived in the NASA Planetary Data System’s Planetary Plasma Interactions Node at <https://pds-ppi.igpp.ucla.edu/> and also available through the CRaTER website at <https://crater-products.sr.unh.edu/data/inst/12/>. The Wind spacecraft solar wind and magnetic field data are provided on the Wind website at [https://wind.nasa.gov/mfi\\_swe\\_plot.php](https://wind.nasa.gov/mfi_swe_plot.php). STEREO heliospheric imager observations and derived data are available on the HELCATS (<https://www.helcats-fp7.eu/>) and Helio4Cast (<https://helioforecast.space/arrcat>) websites. Graduated cylindrical shell reconstruction of CMEs was performed using version 0.2.0 of a new Python implementation of the GCS model (<https://doi.org/10.5281/zenodo.4443203>) available at [https://github.com/johan12345/gcs\\_python](https://github.com/johan12345/gcs_python), which is based on version 2.0.3 (<https://doi.org/10.5281/zenodo.4065067>) of the SunPy open source software package (The SunPy Community et al. 2020) and coronagraph images provided by the Helioviewer.org API (Müller et al. 2017).

## References

- Abunin, A., Abunina, M., Belov, A., et al. 2013, in International Cosmic Ray Conference, Vol. 33, International Cosmic Ray Conference, 1618
- Abunina, M. A., Belov, A. V., Eroshenko, E. A., et al. 2020, *Sol. Phys.*, 295, 69
- Agostinelli, S., Allison, J., Amako, K., et al. 2003, *Nuclear Instruments and Methods in Physics Research Section A: Accelerators, Spectrometers, Detectors and Associated Equipment*, 506, 250
- Alzate, N. & Morgan, H. 2017, *The Astrophysical Journal*, 840, 103
- Appel, J. K. 2018, PhD thesis, University of Kiel
- Appel, J. K., Köhler, J., Guo, J., et al. 2018, *Earth and Space Science*, 5, 2
- Asvestari, E., Gil, A., Kovaltsov, G. A., & Usoskin, I. G. 2017, *Journal of Geophysical Research (Space Physics)*, 122, 9790
- Barnes, D., Davies, J. A., Harrison, R. A., et al. 2019, *Solar Physics*, 294
- Belov, A. 2000, *Space Sci. Rev.*, 93, 79
- Belov, A., Abunin, A., Abunina, M., et al. 2015, *Sol. Phys.*, 290, 1429
- Belov, A., Eroshenko, E., Yanke, V., et al. 2018, *Sol. Phys.*, 293, 68
- Belov, A. V., Blokh, I. L., Dorman, L. I., et al. 1974, *Akademiia Nauk SSSR Izvestiia Seriya Fizicheskaya*, 38, 1867
- Belov, A. V., Blokh, Y. A., Dorman, L. I., et al. 1973, in International Cosmic Ray Conference, Vol. 2, International Cosmic Ray Conference, 1247
- Bothmer, V. & Schwenn, R. 1998, *Annales Geophysicae*, 16, 1
- Brueckner, G. E., Howard, R. A., Koomen, M. J., et al. 1995, *Solar Physics*, 162, 357
- Cane, H. V. 2000, *Space Science Reviews*, 93, 55
- Cane, H. V., Richardson, I. G., von Roseninge, T. T., & Wibberenz, G. 1994, *Journal of Geophysical Research: Space Physics*, 99, 21429
- Clem, J. M. & Dorman, L. I. 2000, *Space Science Reviews*, 93, 335
- Corti, C., Potgieter, M. S., Bindi, V., et al. 2019, *The Astrophysical Journal*, 871, 253
- Davies, E., Möstl, C., Weiss, A. J., & et al. 2021, *Astronomy & Astrophysics*, submitted (not yet accepted)
- Davies, J. A., Harrison, R. A., Perry, C. H., et al. 2012, *The Astrophysical Journal*, 750, 23
- Démoulin, P. & Dasso, S. 2009, *A&A*, 498, 551
- Démoulin, P., Nakwacki, M. S., Dasso, S., & Mandrini, C. H. 2008, *Solar Physics*, 250, 347
- Dorman, L. 2009, *Cosmic Rays in Magnetospheres of the Earth and other Planets*, Vol. 358 (Springer)
- Dumbović, M., Heber, B., Vršnak, B., Temmer, M., & Kirin, A. 2018, *The Astrophysical Journal*, 860, 71
- Dumbović, M., Vršnak, B., Guo, J., et al. 2020, *Solar Physics*, 295, 104
- Forbush, S. E. 1937, *Phys. Rev.*, 51, 1108
- Freiherr von Forstner, J. L., Guo, J., Wimmer-Schweingruber, R. F., et al. 2020, *Journal of Geophysical Research: Space Physics*, 125, e2019JA027662
- Freiherr von Forstner, J. L., Guo, J., Wimmer-Schweingruber, R. F., et al. 2018, *Journal of Geophysical Research: Space Physics*, 123, 39
- Freiherr von Forstner, J. L., Guo, J., Wimmer-Schweingruber, R. F., et al. 2019, *Space Weather*, 17, 586
- Gieseler, J. & Heber, B. 2016, *Astronomy & Astrophysics*, 589, A32
- Gieseler, J., Heber, B., & Herbst, K. 2017, *Journal of Geophysical Research (Space Physics)*, 122, 10,964
- Gopalswamy, N. 2008, *Journal of Atmospheric and Solar-Terrestrial Physics*, 70, 2078, coupling of Solar Wind, Magnetosphere, Ionosphere and Upper Atmosphere
- Guliano, A. M., Démoulin, P., Dasso, S., & Rodríguez, L. 2012, *A&A*, 543, A107
- Guo, J., Wimmer-Schweingruber, R. F., Dumbović, M., Heber, B., & Wang, Y. 2020, *Earth and Planetary Physics*, 4, 62
- Hassler, D. M., Zeitlin, C., Wimmer-Schweingruber, R. F., et al. 2012, *Space Science Reviews*, 170, 503
- He, W., Liu, Y. D., Hu, H., Wang, R., & Zhao, X. 2018, *The Astrophysical Journal*, 860, 78
- Horbury, T. S., O’Brien, H., Blazquez, I. C., et al. 2020, *Astronomy & Astrophysics*
- Howard, R. A., Moses, J. D., Vourlidas, A., et al. 2008, *Space Science Reviews*, 136, 67
- Howard, T. A. & Harrison, R. A. 2013, *Solar Physics*, 285, 269
- Janvier, M., Winslow, R. M., Good, S., et al. 2019, *Journal of Geophysical Research: Space Physics*, 124, 812
- Kilpua, E., Koskinen, H. E. J., & Pulkkinen, T. I. 2017, *Living Reviews in Solar Physics*, 14, 5
- Koldobskiy, S. A., Kovaltsov, G. A., & Usoskin, I. G. 2018, *Sol. Phys.*, 293, 110
- Krymsky, G. 1964, *Geomagn. Aeronomy*, 4, 763
- Krymsky, G., Altukhov, A., Kuzmin, A., & Skripin, G. 1966, *A New Method for Studying the Anisotropy of Cosmic Rays—Investigation of Geomagnetism and Aeronomy (Nauka, Moscow)*
- Kühl, P., Banjac, S., Heber, B., et al. 2015, *Central European Astrophysical Bulletin*, 39, 119

- Lawrence, D. J., Peplowski, P. N., Feldman, W. C., Schwadron, N. A., & Spence, H. E. 2016, *Journal of Geophysical Research (Space Physics)*, 121, 7398
- Leitner, M., Farrugia, C. J., Möstl, C., et al. 2007, *Journal of Geophysical Research: Space Physics*, 112
- Lemen, J. R., Title, A. M., Akin, D. J., et al. 2012, *Solar Physics*, 275, 17
- Lepping, R. P., Acuña, M. H., Burlaga, L. F., et al. 1995, *Space Science Reviews*, 71, 207
- Lockwood, J. A. 1971, *Space Science Reviews*, 12, 658
- Lockwood, J. A., Webber, W. R., & Debrunner, H. 1991, *Journal of Geophysical Research: Space Physics*, 96, 5447
- Looper, M. D., Mazur, J. E., Blake, J. B., et al. 2013, *Space Weather*, 11, 142
- Ma, S., Attrill, G. D. R., Golub, L., & Lin, J. 2010, *The Astrophysical Journal*, 722, 289
- Manchester, IV, W. B., Gombosi, T. I., Zeeuw, D. L. D., et al. 2005, *The Astrophysical Journal*, 622, 1225
- McDonald, F. B. & Ludwig, G. H. 1964, *Physical Review Letters*, 13, 783
- Müller, D., Cyr, O. S., Zouganelis, I., et al. 2020, *Astronomy & Astrophysics*
- Müller, D., Marsden, R. G., St. Cyr, O. C., & Gilbert, H. R. 2013, *Solar Physics*, 285, 25
- Müller, D., Nicula, B., Felix, S., et al. 2017, *A&A*, 606, A10
- Möstl, C., Amerstorfer, T., Palmerio, E., et al. 2018, *Space Weather*, 16, 216
- Möstl, C., Isavnin, A., Boakes, P. D., et al. 2017, *Space Weather*, 15, 955
- Ogilvie, K. W., Chornay, D. J., Fritzenreiter, R. J., et al. 1995, *Space Science Reviews*, 71, 55
- Owen, C. J., Bruno, R., Livi, S., Louarn, P., & Janabi, K. A. 2020, *Astronomy & Astrophysics*
- Papaioannou, A., Belov, A., Abunina, M., et al. 2020, *ApJ*, 890, 101
- Papaioannou, A., Belov, A., Abunina, M., et al. 2019, *Sol. Phys.*, 294, 66
- Potgieter, M. S. 2013, *Living Reviews in Solar Physics*, 10, 3
- Potgieter, M. S., Vos, E. E., Boezio, M., et al. 2014, *Solar Physics*, 289, 391
- Reames, D. V. 2013, *Space Science Reviews*, 175, 53
- Richardson, I. G. & Cane, H. V. 2011, *Sol. Phys.*, 270, 609
- Richardson, I. G., Wibberenz, G., & Cane, H. V. 1996, *Journal of Geophysical Research: Space Physics*, 101, 13483
- Rodríguez-Pacheco, J., Wimmer-Schweingruber, R. F., Mason, G. M., et al. 2020, *A&A*, 642, A7
- Schwadron, N. A., Baker, T., Blake, B., et al. 2012, *Journal of Geophysical Research: Planets*, 117
- Simpson, J. A. 1983, *Annual Review of Nuclear and Particle Science*, 33, 323
- Siscoe, G. & Odstreil, D. 2008, *Journal of Geophysical Research: Space Physics*, 113
- Smart, D. & Shea, M. 2008, in *Proceedings of the 30th International Cosmic Ray Conference*, Vol. 1, 737–740
- Sohn, J., Oh, S., Yi, Y., & Lee, J. 2019a, *Journal of Korean Physical Society*, 74, 614
- Sohn, J., Oh, S., Yi, Y., & Lee, J. 2019b, *Astrophysics and Space Science*, 364, 125
- Spence, H. E., Case, A. W., Golightly, M. J., et al. 2010, *Space Science Reviews*, 150, 243
- The SunPy Community, Barnes, W. T., Bobra, M. G., et al. 2020, *The Astrophysical Journal*, 890, 68
- Thernisien, A. 2011, *The Astrophysical Journal Supplement Series*, 194, 33
- Thernisien, A., Howard, R. A., & Vourlidas, A. 2006, *The Astrophysical Journal*, 652, 763
- Usoskin, I. G., Bazilevskaya, G. A., & Kovaltsov, G. A. 2011, *Journal of Geophysical Research (Space Physics)*, 116, A02104
- Webber, W. R. & Lockwood, J. A. 1999, *Journal of Geophysical Research*, 104, 2487
- Weiss, A. J., Möstl, C., Amerstorfer, T., et al. 2020, *arXiv e-prints*, arXiv:2009.00327
- Wimmer-Schweingruber, R. F., Yu, J., Böttcher, S. I., et al. 2020, *Space Science Reviews*, 216
- Winslow, R. M., Schwadron, N. A., Lugaz, N., et al. 2018, *The Astrophysical Journal*, 856, 139
- Witasse, O., Sánchez-Cano, B., Mays, M. L., et al. 2017, *Journal of Geophysical Research: Space Physics*, 122, 7865, 2017JA023884
- 
- <sup>1</sup> Institut für Experimentelle und Angewandte Physik, Christian-Albrechts-Universität zu Kiel, 24098 Kiel, Germany  
e-mail: forstner@physik.uni-kiel.de
- <sup>2</sup> Hvar Observatory, Faculty of Geodesy, University of Zagreb, Zagreb, Croatia
- <sup>3</sup> Space Research Institute, Austrian Academy of Sciences, Graz, Austria
- <sup>4</sup> School of Earth and Space Sciences, University of Science and Technology of China, Hefei, China
- <sup>5</sup> CAS Center for Excellence in Comparative Planetology, Hefei, PR China
- <sup>6</sup> Institute for Astronomy, Astrophysics, Space Applications and Remote Sensing (IAASARS), National Observatory of Athens, Athens, Greece
- <sup>7</sup> Space Research Group, Universidad de Alcalá, 28805 Alcalá de Henares, Spain
- <sup>8</sup> Pushkov Institute of Terrestrial Magnetism, Ionosphere, and Radio Wave Propagation, Russian Academy of Sciences (IZMIRAN), Troitsk, Moscow, Russia
- <sup>9</sup> Imperial College London, London SW7 2AZ, United Kingdom
- <sup>10</sup> Johns Hopkins University Applied Physics Laboratory, Laurel, MD, United States
- <sup>11</sup> Now at: DSI Datensicherheit GmbH, Rodendamm 34, 28816 Stuhr
- <sup>12</sup> Now at: Deutsches Elektronen-Synchrotron (DESY), Platanenallee 6, 15738 Zeuthen, Germany
- <sup>13</sup> Now at: Department of Extrasolar Planets and Atmospheres, German Aerospace Center (DLR), Berlin, Germany
- <sup>14</sup> Now at: Max-Planck-Institute for Solar System Research, Justus-von-Liebig-Weg 3, 37077 Göttingen, Germany
- <sup>15</sup> Laboratory for Atmospheric and Space Physics, University of Colorado Boulder, Boulder, CO, USA